



Amplitude analysis of the radiative decay $B_s^0 \rightarrow K^+ K^- \gamma$

LHCb collaboration[†]

Abstract

A search for radiative decay of B_s^0 mesons to orbitally excited $K^+ K^-$ states is performed using proton proton collisions recorded by the LHCb experiment, corresponding to an integrated luminosity of 9 fb^{-1} . The dikaon spectrum in the mass range $m_{KK} < 2400 \text{ MeV}/c^2$ is dominated by the $\phi(1020)$ resonance that accounts for almost 70% of the decay rate. Considering the possible contributions of $f_2(1270)$, $f_2'(1525)$ and $f_2(2010)$ meson states, the overall tensor contribution to the amplitude is measured to be

$$\mathcal{F}_{\{f_2\}} = 16.8 \pm 0.5 \text{ (stat.)} \pm 0.7 \text{ (syst.)}\%,$$

mostly dominated by the $f_2'(1525)$ state. Several statistically equivalent solutions are obtained for the detailed resonant structure depending on whether the smaller amplitudes interfere destructively or constructively with the dominant amplitude. The preferred solution that corresponds to the lowest values of the fit fractions along with constructive interference leads to the relative branching ratio measurement

$$\frac{\mathcal{B}(B_s^0 \rightarrow f_2' \gamma)}{\mathcal{B}(B_s^0 \rightarrow \phi \gamma)} = 19.4_{-0.8}^{+0.9} \text{ (stat.)}_{-0.5}^{+1.4} \text{ (syst.)} \pm 0.5 \text{ (}\mathcal{B}\text{)}\%,$$

where the last uncertainty is due to the ratio of measured branching fractions to the $K^+ K^-$ final state. This result represents the first observation of the radiative $B_s^0 \rightarrow f_2'(1525) \gamma$ decay, which is the second radiative transition observed in the B_s^0 sector.

Submitted to JHEP

© 2024 CERN for the benefit of the LHCb collaboration. CC BY 4.0 licence.

[†]Authors are listed at the end of this paper.

1 Introduction

In the Standard Model (SM), the radiative decays of beauty hadrons proceed at leading order through $b \rightarrow s\gamma$ one-loop electromagnetic-penguin transitions, dominated by a virtual intermediate top quark coupled to a W boson. Extensions of the SM predict additional one-loop contributions that can introduce sizeable effects on the dynamics of the transition. Radiative decays of the neutral and charged B mesons were first observed by the CLEO collaboration in 1993 [1] through the decay modes $B \rightarrow K^*\gamma$. In 2007 the Belle collaboration reported the first observation of the companion decay in the B_s^0 sector [2], $B_s^0 \rightarrow \phi\gamma$. The LHC era has brought observations of new radiative b -hadron decay modes and precise measurements of branching fractions, helicity structure and asymmetries in this class of decays [3–10].

Several exclusive modes have been observed in radiative decays of neutral B^0 mesons [11], including tensor intermediate states, and compared to theoretical predictions [12–15]. In the B_s^0 sector, the $\phi\gamma$ final state remains the only $b \rightarrow s\gamma$ transition observed. Radiative decays of scalar beauty mesons allow a clean spectroscopic representation of the hadronic system accompanying the photon, free of the S-wave amplitude contributions that usually complicate partial wave analyses.¹ This work represents the first amplitude analysis of the dikaon resonant structure in the $B_s^0 \rightarrow K^+K^-\gamma$ decay² up to a dikaon invariant mass $m_{KK} = 2400 \text{ MeV}/c^2$. This analysis exploits data collected by the LHCb experiment in proton–proton (pp) collisions at 7, 8 and 13 TeV centre-of-mass energies in the years of 2011–2012 (Run 1) and of 2015–2018 (Run 2), corresponding to 3 fb^{-1} and 6 fb^{-1} of integrated luminosity, respectively.

2 Detector and selection

The LHCb detector is a single-arm forward spectrometer covering the pseudorapidity range $2 < \eta < 5$ designed for the study of heavy hadrons containing b or c quarks [17, 18]. The detector elements that are relevant for this analysis are: a silicon-strip vertex detector surrounding the pp interaction region that allows the beauty hadron to be identified from its characteristically long flight distance; a tracking system that provides a precise measurement of the dikaon momentum; two ring-imaging Cherenkov detectors (RICH) that allow to discriminate between the different species of charged hadrons; a calorimeter system consisting of scintillating-pad (SPD) and preshower detectors, an electromagnetic calorimeter (ECAL) and a hadronic calorimeter, that provides the reconstruction and the identification of the radiated photons. In addition, a muon system allows the identification of muons.

Simulated samples are used to optimise the selection criteria and evaluate the background contamination. The simulated pp collisions are generated using Pythia [19, 20]. The decay chain of hadronic particles and the final-state radiation are handled by EvtGen [21] and PHOTOS [22], respectively. The detector response to the interacting particles is implemented in the Geant4 framework [23, 24].

The online event selection is performed by a trigger [25, 26], consisting of a hardware stage based on the information from the calorimeter and muon systems, followed by a

¹A similar feature is realised in the $J/\psi \rightarrow K^+K^-\pi^0$ hadronic decay [16].

²The inclusion of charge-conjugate processes is implicit unless stated otherwise.

software stage which fully reconstructs the event. In order to reduce the large level of combinatorial background coming from pp collisions, the hardware trigger selects events having an ECAL cluster with an energy component transverse to the beam (E_T) above a threshold varying between 2.50 and 2.96 (2.11 and 2.70) GeV in Run 1 (Run 2). To facilitate the reconstruction in the software trigger the hardware trigger selects only events with fewer than 600 (450) hits in the SPD for Run 1 (Run 2).

The software trigger is designed to efficiently select candidates with two high transverse momentum (p_T) tracks significantly displaced from the interaction point and one high- E_T photon [27]. The trigger efficiency is further enhanced by about 20% by imposing looser track requirements for the events passing a tighter photon threshold, $E_T > 4$ GeV, at the hardware stage. For Run 2 data, a multivariate classifier based on topological criteria complements the software trigger selection [28]. The Run 1 software trigger requires m_{KK} to be below 2000 MeV/ c^2 . This restrictive criterion has been removed in Run 2 and the dikaon phase space of this analysis is extended up to $m_{KK} < 2400$ MeV/ c^2 , corresponding to the observed phase space of the $B_s^0 \rightarrow K^+K^-\gamma$ signal. A fiducial cut $m_{KK} < 1950$ MeV/ c^2 , just below the trigger threshold, is applied to the Run 1 data.

The reconstructed $B_s^0 \rightarrow K^+K^-\gamma$ candidate combines a pair of good-quality tracks and an energetic photon. The two tracks are required to have large impact parameters (IP) with a significance that exceeds four units with respect to any reconstructed interaction vertex. Both tracks must have a transverse momentum larger than 500 MeV/ c with at least one above 1.2 GeV/ c . Kaons are identified using particle identification information provided mainly by the RICH system. The probability associated to the kaon hypothesis must be larger than any other hadron hypothesis, pion or proton, and larger than a threshold optimised to reduce the expected contamination from $B^0 \rightarrow K^+\pi^-\gamma$ and $\Lambda_b^0 \rightarrow pK^-\gamma$ radiative decays, which have the same topology as the signal. The optimisation is performed for each year of data taking using simulated samples with particle identification performance derived from dedicated calibration data. The fiducial ranges used for track momentum, $p \in [4.5, 100.0]$ GeV/ c , and pseudorapidity, $\eta \in [1.5, 4.5]$, match the phase space covered by the data-driven calibration tool [29]. The two tracks should have a distance of closest approach less than 0.15 mm and form a good quality vertex. Vertex isolation is used to reduce partially reconstructed $B \rightarrow K^+K^-(X)\gamma$ backgrounds, where X generically represents an unreconstructed fragment of the decay final state. Specifically, a lower limit is applied on the χ^2 increase in the vertex fit when adding any additional reconstructed track, referred to in the following as $\Delta\chi_{\text{Vtx}}^2(B_s^0)$.

Clusters in the ECAL system identified as photon candidates are selected by requiring that they cannot be geometrically associated with any extrapolated track. Photons and neutral pions are distinguished by exploiting their cluster shape and energy distribution [30]. The photon four-momentum is evaluated using the dikaon vertex as the origin and the position and energy of the associated cluster. The transverse component of the reconstructed photon momentum is required to be larger than 3.0 GeV/ c .

The B_s^0 candidate four-momentum is computed by summing the four-momenta of the two kaons and the photon. The B_s^0 candidates are selected in the mass range [4700, 6400] MeV/ c^2 . The momentum is required to point back to the associated primary vertex (PV) and to have a transverse component larger than 2.0 GeV/ c . A significant contamination is expected from the $B_{(s)}^0 \rightarrow (K^\pm\pi^0)K^\mp$ decays that involve a $K^\pm\pi^0$ resonant state, including charmed modes through $D_{(s)}^\pm$ decays. Those hadronic contributions are

vetoed by requiring the $K^\pm\gamma$ system to be above the D_s^\pm mass, *i.e.* $m_{K^\pm\gamma} > 2000 \text{ MeV}/c^2$, assigning the neutral pion mass to the reconstructed photon. This criterion, hereafter referred to as the anti-charm veto, suppresses the mass peaking contamination from charmless $B^0 \rightarrow K^{*\pm}K^\mp$ decays and significantly reduces the partially reconstructed decays involving a misidentified π^0 meson.

Background candidates resulting from combinations of unrelated kaons and photon, hereafter denoted as combinatorial background, can be strongly suppressed by exploiting kinematic and topological variables. Boosted Decision Tree classifiers (BDT) [31, 32] are trained for each year of data taking using simulated events reproducing the detector conditions as signal proxy and data selected in the upper mass sideband of the signal mass peak as background proxy. The typical mass resolution of the $B_s^0 \rightarrow K^+K^-\gamma$ signal is $85 \text{ MeV}/c^2$, and is dominated by the photon energy resolution. The upper mass sideband is accordingly defined as $m_{K^+K^-\gamma} > m_{B_s^0} + 300 \text{ MeV}/c^2$. The input variables to the classifier are: the momentum, pseudorapidity, flight distance and $\Delta\chi_{\text{Vtx}}^2(B_s^0)$ of the reconstructed B_s^0 candidate, the IP and transverse momentum of the kaon candidates, the IP, momentum, and p_T of the dikaon combination, and the difference of the primary vertex fit χ^2 calculated with or without the tracks associated to the reconstructed B_s^0 meson. An additional input variable to the BDT in Run 2 is the isolation variable,

$$I_{p_T} = \frac{p_T(B_s^0) - \sum p_T}{p_T(B_s^0) + \sum p_T}, \quad (1)$$

where the sum is taken over tracks that are not part of the B_s^0 signal candidate but are associated with the same PV and fall within a cone of half-angle $\Delta R < 1.7$ rad. The half-angle of a track is defined as $(\Delta R)^2 = (\Delta\theta)^2 + (\Delta\phi)^2$, where $\Delta\theta$ and $\Delta\phi$ are the differences in the polar and azimuthal angles of each track with respect to the B_s^0 candidate direction. The optimal BDT working point is optimised for each year of data taking by maximising the ratio $S/\sqrt{S+B}$, where S is the expected number of signal candidates estimated from simulation and B is the number of combinatorial background candidates in the signal region estimated by extrapolating the data distribution in the upper mass sideband of the signal mass peak. The efficiency of the optimal BDT cut on the preselected signal is around 97% while the combinatorial background is reduced by factor of 20.

The remaining combinatorial background and the partially reconstructed B decays can be constrained by their invariant-mass distribution on both sides of the signal peak. The selected $K^+K^-\gamma$ sample is additionally polluted by misidentified $B^0 \rightarrow K^+\pi^-\gamma$ and $\Lambda_b^0 \rightarrow pK^-\gamma$ decays that pass the dikaon identification requirements and populate the B_s^0 signal region. The corresponding B^0 and Λ_b^0 contamination estimated from simulation are $4.5 \pm 1.1\%$ and $6.9 \pm 1.9\%$ of the signal yield, respectively. Due to the limited calorimeter energy resolution and the resulting wide signal peak, the misidentified backgrounds cannot be efficiently separated from the B_s^0 signal mass distribution. Further peaking backgrounds stemming from photon misidentification, such as $B \rightarrow K^+K^-\pi^0$ charmless decays, are highly suppressed thanks to the anti-charm veto that rejects the $K^{*\pm}K^\mp$ intermediate states. The residual colour-suppressed decay modes to the $(K^+K^-\pi^0)$ final states are difficult to quantify due to their unknown resonant structure. The suppressed charmed decay $B^0 \rightarrow \bar{D}^0\pi^0$ with $\bar{D}^0 \rightarrow K^+K^-$ or $K^+\pi^-$, which is well-localized in the dikaon mass spectrum, can similarly contribute to the signal mass region. The unresolved peaking

contributions are, therefore, embedded in the signal component in the mass model and their description is handled in the subsequent amplitude analysis of the dikaon system.

3 Invariant mass fit

The invariant-mass distribution of the $B_s^0 \rightarrow K^+K^-\gamma$ signal is modelled using a modified double-sided Crystal-Ball [33] probability density function (PDF) with an asymmetrical Gaussian core and tails on either side. The Gaussian mass peak position and the left/right width parameters are allowed to vary freely in the fit to accommodate the possible difference between simulation and data resolutions and to account for the contamination of the embedded peaking backgrounds. The low-mass tail parameters cannot be resolved in the fit to data due to the large partially reconstructed backgrounds populating the left sideband. They are fixed to the values obtained from a fit to simulated samples. The high-mass tail accounts for the imperfections of the tracking and, in the case of radiative decays, the large cluster pile-up variations in the ECAL which may affect the photon energy determination. The parameter that defines the right-tail transition point is allowed to vary freely in the fit to adjust the misidentified $\Lambda_b^0 \rightarrow pK^-\gamma$ background, mostly contaminating the right side of the signal peak, while the tail decay parameter is fixed to the value obtained from simulation. The partially reconstructed $B_s^0 \rightarrow K^+K^-(X)\gamma$ backgrounds are described using ARGUS functions [34] convoluted with the signal resolution function. Two inclusive components, with one or with two missing pions, are considered for the partially reconstructed B_s^0 decays in the nominal mass range, $m_{KK\gamma} \in [4700, 6400]$ MeV/ c^2 . Several exclusive decay modes with similar shapes potentially compete in the partially reconstructed decay region. Furthermore, the branching fractions of most of these decays are unknown. The overall yield of the inclusive partially reconstructed contributions, hereafter denoted as one-missing-pion and two-missing-pion components, is thus allowed to vary freely in the fit to data. The shape of the one-missing-pion component is partially constrained using the parameterisation obtained from a fit to the simulated decay $B_s^0 \rightarrow \phi(1680)(\rightarrow K^+K^-\pi^0)\gamma$, used as a proxy. In the fit to data, the curvature parameter of the ARGUS function is fixed to the value obtained from the fit to this simulated sample. The missing-mass shift is set to the known neutral pion mass [11], m_{π^0} , and the slope parameter, which depends on the actual decay dynamics, is allowed to vary freely to accommodate the unknown composition of the generic one-missing-pion component. The two-missing-pion component, which mostly contributes to the lower edge of the mass window, is modelled using a similar ARGUS function, with a missing-mass shift fixed to $2m_{\pi^0}$ and a free slope parameter. The curvature parameter, poorly resolved in the fit to data, is fixed to the same value as for the one-missing-pion component. The combinatorial background due to random $KK\gamma$ combinations is modelled using a decreasing exponential shape where the decay parameter is free to vary. The peaking backgrounds are not modelled separately and are included in the signal component, as previously discussed.

An unbinned extended maximum-likelihood fit is performed according to the PDF

$$\mathcal{F}(m_{KK\gamma}) = N_s \cdot S(m_{KK\gamma}) + \sum_{\text{BKG}} N_{\text{BKG}} \cdot B_{\text{BKG}}(m_{KK\gamma}), \quad (2)$$

where S (B_{BKG}) represents the signal (background) PDF and N_s (N_{BKG}) the associated yield(s) allowed to vary freely. The resulting fit projections on the Run 1 and Run 2 data

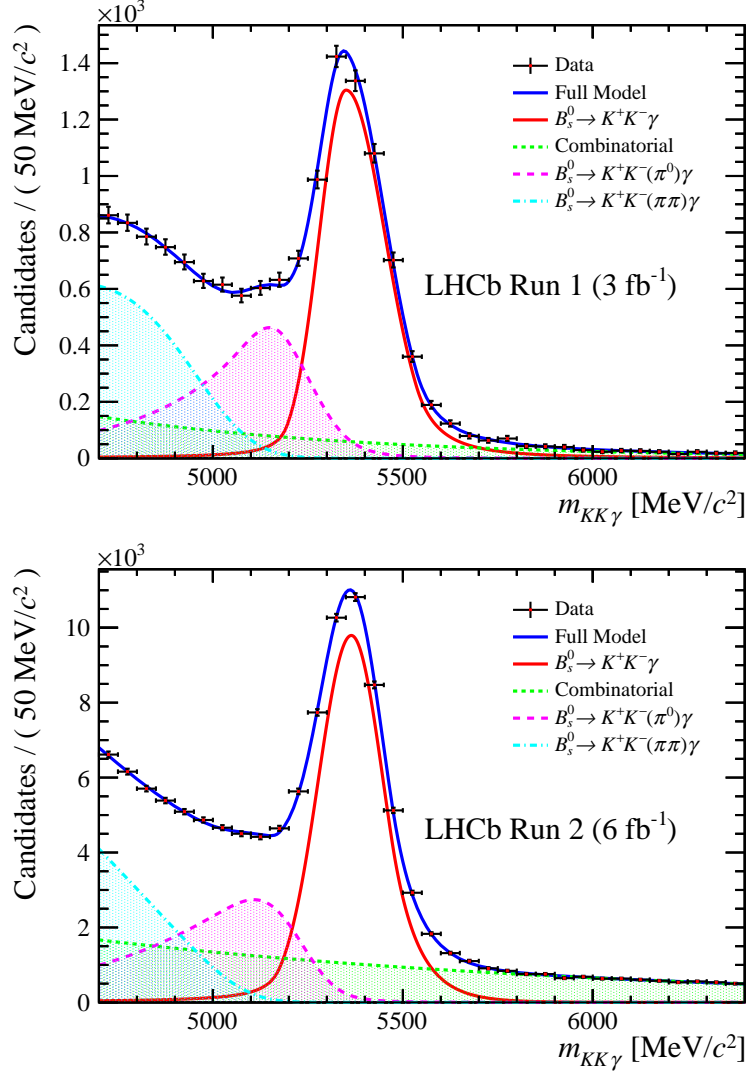


Figure 1: Invariant-mass distribution for $K^+K^-\gamma$ candidates for (top) Run 1 and (bottom) Run 2, with the fit projection overlaid.

samples are shown in Fig. 1. The yield of the $B_s^0 \rightarrow K^+K^-\gamma$ signal candidates is found to be $N_s = (5.66 \pm 0.14) \times 10^3$ and $(44.5 \pm 0.5) \times 10^3$ in Run 1 and Run 2, respectively, including peaking background components that are expected to contribute about 10%.

Following the $s\mathcal{P}$ lot technique [35], a signal weight ($s\mathcal{W}$ eight) is assigned to each candidate to statistically subtract the combinatorial and partially reconstructed background components in the subsequent amplitude analysis. The left-hand plot in Fig. 2 displays the dikaon mass distribution for the selected $K^+K^-\gamma$ candidates. The $s\mathcal{W}$ eighted projection of the signal component that contributes up to $m_{KK} \sim 2400$ MeV/ c^2 is superimposed. The right-hand plot in Fig. 2 displays the signal $s\mathcal{W}$ eighted projection on the amplitude observables plane ($m_{KK}, \cos\theta_{KK}$), where θ_{KK} is the helicity angle defined as the angle between the positively charged kaon direction and the B_s^0 meson momentum in the dikaon rest frame. Aside from the dominant vector contribution in the $\phi(1020)$ region, one can clearly see a tensor contribution around 1500 MeV/ c^2 , identifiable as a significant contribution from the $f_2'(1525)$ resonance.

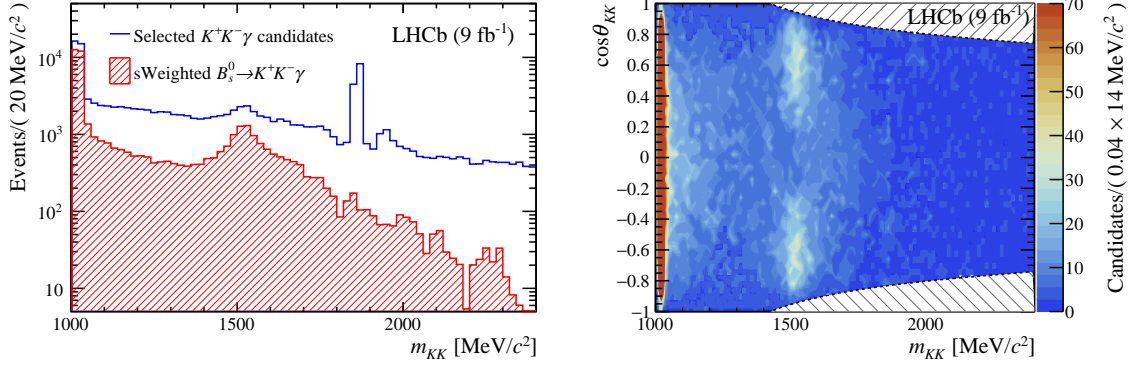


Figure 2: (Left) dikaon invariant mass for the selected $K^+K^-\gamma$ candidates and the sWeighted signal distribution. The narrow peak around 1860 MeV/c² and its small reflection 100 MeV/c² above correspond to $D^0 \rightarrow K^+K^-$ and to misidentified $D^0 \rightarrow K^-\pi^+$ decays, which are strongly suppressed in the sWeighted distribution. (Right) sWeighted projection of the $B_s^0 \rightarrow K^+K^-\gamma$ signal on the $(m_{KK}, \cos\theta_{KK})$ plane. The hatched areas indicate the acceptance regions suppressed by the anti-charm veto (see Sect. 4.2 for details).

4 Amplitude analysis

4.1 Amplitude model

The kinematics of the three-body transition $B_s^0 \rightarrow (K^+K^-)_R\gamma$, where R is an intermediate dikaon state, can be completely described by the invariant dikaon mass, m_{KK} , and the helicity observable, $\cos\theta_{KK}$, related to the traditional Dalitz [36] mass coordinates $s_{ij} = m_{ij}^2$ as

$$\cos\theta_{KK} = \frac{(s_{K^+\gamma} - s_{K^-\gamma})m_{KK}}{4M_{B_s^0}q_Rq_{B_s^0}}c^2, \quad (3)$$

where q_R and $q_{B_s^0}$ represent the kaon momentum in the dikaon rest frame and the dikaon momentum in the B_s^0 rest frame, respectively. The Lorentz-invariant three-body decay rate in the $(m_{KK}, \cos\theta_{KK})$ coordinates system is given by

$$d\Gamma = \mathcal{J}_3(m_{KK})|\mathcal{M}(m_{KK}, \cos\theta_{KK})|^2 dm_{KK} d\cos\theta_{KK}, \quad (4)$$

where $\mathcal{J}_3(m_{KK})$ represents the three-body phase-space Jacobian³

$$\mathcal{J}_3(m_{KK}) \propto \frac{q_R q_{B_s^0}}{M_{B_s^0}^2} c^{-2}, \quad (5)$$

and the matrix element $\mathcal{M}(m_{KK}, \cos\theta_{KK})$ represents the transition amplitude. The transition probability is obtained by summing incoherently over the unobserved photon helicity states

$$|\mathcal{M}|^2 = \sum_{\lambda=\pm 1} |\mathcal{M}_\lambda|^2 = 2|\mathcal{M}_{|\lambda|=1}|^2, \quad (6)$$

where the last identity results from the fact that $\mathcal{M}_{\lambda=+1}$ exhibits the same θ_{KK} helicity dependency as $\mathcal{M}_{\lambda=-1}$.

³Irrelevant constant factors are omitted here.

To describe this amplitude transition, an isobar approach is used that consists of the coherent sum of the individual amplitudes describing the intermediate states

$$\mathcal{M}(m_{KK}, \cos \theta_{KK}) = \sum_{\mathbf{R}} c_{\mathbf{R}} \mathcal{A}_{\mathbf{R}}(m_{KK}, \cos \theta_{KK}), \quad (7)$$

where $c_{\mathbf{R}}$ is a complex coefficient and $\mathcal{A}_{\mathbf{R}}$ represents the amplitude for the intermediate state \mathbf{R} . The amplitudes $\mathcal{A}_{\mathbf{R}}$ are modelled as

$$\mathcal{A}_{\mathbf{R}}(m_{KK}, \cos \theta_{KK}) = A_{\mathbf{R}}(m_{KK}) d_{\lambda\lambda'}^{J_{\mathbf{R}}}(\cos \theta_{KK}), \quad (8)$$

where $A_{\mathbf{R}}(m_{KK})$ is the mass lineshape of the intermediate state \mathbf{R} with spin $J_{\mathbf{R}}$. The angular dependency is given by the Wigner d-functions $d_{\lambda\lambda'}^{J_{\mathbf{R}}}(\theta_{KK})$ that represent the matrix elements of the operator rotating the angular momentum basis from the B_s^0 decay axis ($|\lambda| = 1$) to the dikaon decay axis ($\lambda' = 0$) [37]. As no S-wave is allowed in the radiative decays of B mesons, a nominal model based on relativistic Breit–Wigner amplitudes is adopted to describe the mass lineshapes, $A_{\mathbf{R}}(m_{KK})$, for all the considered resonant states

$$A_{\mathbf{R}}(m_{KK}) = \mathcal{F}_{\mathbf{R}} \cdot \mathcal{F}_B \cdot \mathcal{BW}_{\mathbf{R}}(m_{KK}; \mu_{\mathbf{R}}, \Gamma_{\mathbf{R}}), \quad (9)$$

where $\mathcal{F}_{\mathbf{R}}$ and \mathcal{F}_B are the Blatt–Weiskopf factors [38] accounting for the centrifugal barrier effect in the decays of the \mathbf{R} resonance and the B_s^0 meson, respectively. The Breit–Wigner complex pole for the resonance \mathbf{R} is given by

$$\mathcal{BW}_{\mathbf{R}}(m_{KK}; \mu_{\mathbf{R}}, \Gamma_{\mathbf{R}}) = \frac{1}{(\mu_{\mathbf{R}}^2 - m_{KK}^2) - i\mu_{\mathbf{R}}\mathcal{W}(m_{KK}; \Gamma_{\mathbf{R}})}, \quad (10)$$

with $\mu_{\mathbf{R}}$ and $\Gamma_{\mathbf{R}}$, are the corresponding pole mass and width. The mass-dependent width is defined as

$$\mathcal{W}(m_{KK}; \Gamma_{\mathbf{R}}) = \Gamma_{\mathbf{R}} \frac{q_{\mathbf{R}}}{\bar{q}_{\mathbf{R}}} \frac{\mu_{\mathbf{R}}}{m_{KK}} \mathcal{F}_{\mathbf{R}}^2, \quad (11)$$

where $\bar{q}_{\mathbf{R}}$ is a reference kaon momentum evaluated at the nominal mass pole of the resonance. The normalized Blatt–Weiskopf form-factors

$$\mathcal{F}_{\mathbf{R}} = \mathcal{F}(q_{\mathbf{R}}, \bar{q}_{\mathbf{R}}, L_{\mathbf{R}}), \quad (12)$$

$$\mathcal{F}_B = \mathcal{F}(q_B, \bar{q}_B, L_B), \quad (13)$$

are derived from the spherical Hankel functions of first kind [38],

$$\mathcal{F}(q, \bar{q}, L) = \left| \frac{\mathcal{H}_L(r\bar{q})}{\mathcal{H}_L(rq)} \right| = \left(\frac{q}{\bar{q}} \right)^L \frac{h_L(r\bar{q})}{h_L(rq)}, \quad (14)$$

where the parameter r is the meson radius that accounts for the size of the centrifugal barrier effect and L is the relative angular momentum in the resonance decay. The L -dependent functions $h_L(z)$ for $L \leq 4$ are

$$h_0(z) = 1, \quad (15)$$

$$h_1(z) = \sqrt{1 + z^2}, \quad (16)$$

$$h_2(z) = \sqrt{9 + 3z^2 + z^4}, \quad (17)$$

$$h_3(z) = \sqrt{225 + 45z^2 + 6z^4 + z^6}, \quad (18)$$

$$h_4(z) = \sqrt{11025 + 1575z^2 + 135z^4 + 10z^6 + z^8}. \quad (19)$$

The radius parameter associated with the $\phi(1020)$ meson lineshape, r_ϕ , is allowed to vary in the fit. The radius value is fixed to $r_{f_2} = 3.0$ (GeV/c) $^{-1}$ for heavier dikaon resonances, and to $r_B = 5.0$ (GeV/c) $^{-1}$ for the B_s^0 meson. The variation of the radii of heavy mesons is considered when evaluating systematic uncertainties. The relative angular momentum L_R of the pseudoscalar kaons equals the resonance spin. The relative angular momentum of the resonance in the radiative B_s^0 decay takes eigenvalues in the $J_R \pm 1$ range. The lowest allowed value, $J_R - 1$, is assumed in the nominal model. Other values are considered when evaluating systematic uncertainties.

The experimental dikaon mass resolution is included in each individual Breit–Wigner pole using an analytical approach derived from Ref. [39] and assuming Gaussian behaviour. The relativistic Voigt profile is built by convoluting the Breit–Wigner profile with a Gaussian resolution function

$$|\mathcal{V}(m; \mu, \Gamma, \sigma)|^2 = \int_{-\infty}^{+\infty} |\mathcal{BW}(m; \mu, \Gamma)|^2 \mathcal{G}(m - m'; 0, \sigma) dm' = \frac{1}{\sigma\sqrt{2\pi}} |\mathcal{H}(a, u_+, u_-)|^2, \quad (20)$$

with $u_\pm = \frac{m \pm \mu}{\sqrt{2}\sigma}$ and $a = \frac{\mu\mathcal{W}(m; \Gamma)}{2\sigma^2}$, and μ and σ representing the Gaussian parameters. The result of the integration is a weighted-sum of Faddeeva functions

$$|\mathcal{H}(a, u_+, u_-)|^2 = \frac{w(z_{++}) + w(z_{+-})}{2\Delta_+} + \frac{w(z_{-+}) + w(z_{--})}{2\Delta_-}, \quad (21)$$

where $z_{\kappa\eta} = (u_+ + u_- + \kappa \cdot \Delta_\eta)/2$, $\Delta_\eta = \sqrt{(u_+ - u_-)^2 + \eta \cdot 4ia}$ and $w(z)$ is the Faddeeva function, *i.e.* the scaled complementary error complex function, the real part of which defines the usual nonrelativistic Voigt profile

$$w(z) = e^{-z^2} \operatorname{erfc}(-iz). \quad (22)$$

The mass resolution is then included in the amplitude model by redefining the Breit–Wigner pole definition as

$$\mathcal{BW}_R(m_{KK}; \mu_R, \Gamma_R, \sigma_R) = |\mathcal{V}(m_{KK}; \mu_R, \Gamma_R, \sigma_R)| e^{i\operatorname{Arg}[\mathcal{B}_R(m_{KK}; \mu_R, \Gamma_R)]}, \quad (23)$$

i.e. the resolution is included in the mass lineshape, but the effect of the resolution on the mass-dependent phase is neglected. The nominal resolution values derived from simulation studies are fixed to $\sigma_\phi = 0.54$ MeV/c 2 for the $\phi(1020)$ lineshape, and to $\sigma_R = 3.2$ MeV/c 2 for all the higher-mass resonances. The experimental resolution on the helicity observable θ_{KK} , found to be negligible over the whole analysis range, is not introduced in the model.

As the K^+K^- system is a CP eigenstate, the flavour of the decaying B_s^0 meson is undefined in this time-integrated analysis. The helicity angle observable in the symmetrical K^+K^- system, θ_H , is univocally defined as the angle between the momentum of the positively-charged kaon and the B_s^0 momentum in the dikaon rest frame. This measured angle matches the helicity angle for one of the B_s^0 flavours, $\theta_H = \theta_{KK}$, but corresponds to the opposite angle, $\theta_H = \pi - \theta_{KK}$, for the opposite flavour. As a consequence, the interference between odd- and even-spin components, which is an anti-symmetrical function of the helicity, cancels out in the case of equal decay rates of the two flavours. Thanks to the fast B_s^0 oscillation, any small flavour asymmetry at the production level [40] is diluted to a negligible level when integrating over time. Assuming, in addition, that there is no violation of the CP symmetry in the penguin-mediated radiative decay [41], an

equal decay rate for B_s^0 and \bar{B}_s^0 is expected. Residual experimental asymmetries due, for instance, to differences in the momentum-dependent K^+/K^- detection efficiencies are explicitly cancelled out by considering the folded ($m_{KK}, |\cos \theta_{KK}|$) half plane and summing incoherently the odd- and even-spin amplitude subsystems. The nominal probability density function describing the signal component is then defined as

$$\mathcal{P}_s(m_{KK}, \theta_{KK}) = \varepsilon(m_{KK}, \theta_{KK}) \cdot \mathcal{J}_3(m_{KK}) \sum_{P=+,-} \left| \sum_{R_P} c_{R_P} \cdot \mathcal{A}_{R_P}(m_{KK}, |\cos \theta_{KK}|) \right|^2, \quad (24)$$

where \mathcal{A}_{R_P} is the amplitude for the component R_P with spin parity P , $c_{R_P} = |c_{R_P}| e^{i\delta_{R_P}}$ is the associated complex isobar coefficient and $\varepsilon(m_{KK}, |\cos \theta_{KK}|)$ is the parametrised experimental acceptance presented in Sect. 4.2.

Including backgrounds, the full PDF describing the selected data sample is given by

$$\mathcal{P}(m_{KK}, \theta_{KK}) = \mathcal{N}_s \cdot \mathcal{P}_s + \sum_{\text{BKG}} \mathcal{N}_{\text{BKG}} \cdot \mathcal{P}_{\text{BKG}}, \quad (25)$$

where \mathcal{N}_s is the overall $(B_s^0 + \bar{B}_s^0) \rightarrow K^+K^-\gamma$ yield, and \mathcal{N}_{BKG} and \mathcal{P}_{BKG} represent the yields and PDFs of the backgrounds, respectively.

4.2 Acceptance

The two-dimensional selection acceptance $\varepsilon(m_{KK}, |\cos \theta_{KK}|)$ is determined from a simultaneous fit to large samples of fully reconstructed $B_s^0 \rightarrow K^+K^-\gamma$ simulated decays, uniformly produced in the decay phase space, $B_s^0 \rightarrow \phi(1020)\gamma$ decays and $B_s^0 \rightarrow f_2'(1525)\gamma$ decays. Weights are applied to the simulated candidates to correct for imperfections in the simulation of kinematic variables and to reproduce the neutral and charged particle identification efficiencies using a data-driven calibration [29, 30].

The PDF that describes each of the simulated samples,

$$\mathcal{P}_R = \varepsilon(m_{KK}, \theta_{KK}; \vec{\alpha}) \cdot \mathcal{J}_3(m_{KK}) \cdot |A_R(m_{KK}) d_{\lambda,0}^{J_R}(\theta_{KK})|^2, \quad (26)$$

embeds the parameterised two-dimensional acceptance function, $\varepsilon(m_{KK}, \theta_{KK}; \vec{\alpha})$. A generic acceptance function based on Bernstein polynomials up to degree 5 is defined as

$$\varepsilon(x, Y; \vec{\alpha}) = 1 + \left[\sum_{i=0}^4 \sum_{j=0}^5 \alpha_{ij} \cdot B_i^4(Y) \cdot B_j^5(X) \right] \cdot \varepsilon_b(m_{KK}, |\cos \theta_{KK}|; \sigma_c), \quad (27)$$

where the coordinate $x = q_r(m_{KK})/q_0$ is the normalized kaon momentum in the dikaon rest frame and $Y = |\cos \theta_{KK}|$ is the folded helicity observable. The functions $B_k^n(u)$ represent the n^{th} -order Bernstein polynomials

$$B_k^n(u) = \binom{n}{k} u^k (1-u)^{n-k}. \quad (28)$$

The normalisation factor $q_0 = q_r(m_{KK}^{\text{max}})$ ensures the Bernstein argument x lies within the $[0, 1]$ bounds for the considered mass range, $m_{KK} \in [2m_K, m_{KK}^{\text{max}}]$. Conditions are applied to the α_{ij} parameters such that the acceptance becomes independent of the undefined

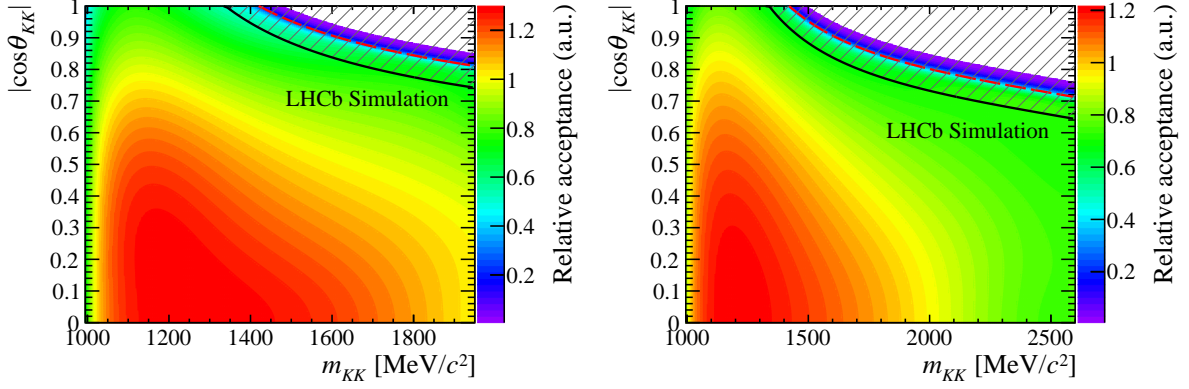


Figure 3: Selection acceptance in the $(m_{KK}, |\cos\theta_{KK}|)$ plane for (left) Run 1 and (right) Run 2. The absolute normalisation $\varepsilon = 1$ is arbitrarily set at the $\phi(1020)$ pole. The dashed-red curves indicate the kinematic boundary corresponding to the anti-charm veto, $m_{K^\pm\gamma\to\pi^0} > 2000$ MeV/ c^2 . The hatched areas delimited by the solid-black curves indicate the fiducial acceptance cut applied to the data.

helicity value at the decay threshold $x = 0$ (implying $\alpha_{i0} = 0, \forall i$) and that the acceptance derivative is continuous on the helicity folding line $y = 0$ (implying $\alpha_{0j} = \alpha_{1j}, \forall j$). These two constraints leave twenty independent α_{ij} parameters to be determined in the fit.

The second factor appearing in the acceptance function of Eq. 27, is defined as

$$\varepsilon_b(m_{KK}, |\cos\theta_{KK}|; \sigma_c) = \frac{1}{2} \left[1 + \operatorname{erf} \left(\frac{c_0(m_{KK}) - |\cos\theta_{KK}|}{\sigma_c} \right) \right], \quad (29)$$

and aims to describe the effect of the anti-charm veto that directly affects the Dalitz acceptance region. This criteria, $m_{K^\pm\gamma\to\pi^0} > m_{\text{cut}}$, is equivalent to a mass-dependent helicity range

$$|\cos\theta_{KK}| < c_0(m_{KK}) \equiv \frac{\left(M_{B_s^0}^2 + 2m_K^2 + m_{\pi^0}^2 - m_{KK}^2 - 2m_{\text{cut}}^2 \right) m_{KK} c^2}{4M_{B_s^0} q_R(m_{KK}) q_B(m_{KK})}, \quad (30)$$

which reaches the physical region, $|\cos\theta_{KK}| \leq 1$ when m_{KK} exceeds ~ 1450 MeV/ c^2 . The error function entered in the definition of the acceptance accounts for the experimental resolution on the upper-limit value, $c_0(m_{KK})$, through the resolution parameter σ_c .

The acceptance is evaluated separately for the Run 1 and Run 2 data samples. The set of acceptance parameters, $\vec{\alpha} = \{\alpha_{ij}, \sigma_c\}$, as well as the mass pole, the width, the reconstructed mass resolution and the meson radius describing the mass shape of the resonances are let free to vary in the fit. The two-dimensional acceptance extracted from the simultaneous fit to the simulated samples is displayed in Fig. 3 for Run 1 and Run 2. The helicity boundary resolution is found to be $\sigma_c^{\text{fit}} = (2.17 \pm 0.07) \times 10^{-2}$ for Run 1 and $\sigma_c^{\text{fit}} = (2.55 \pm 0.03) \times 10^{-2}$ for Run 2. To avoid any systematic effect due to the modelling of the acceptance boundary on data, a fiducial cut, located $3\sigma_c^{\text{fit}}$ below the theoretical threshold, $|\cos\theta_{KK}| < c_0(m_{KK}) - 3\sigma_c^{\text{fit}}$, is applied on the data sample, rejecting less than 1% of the selected signal. The corresponding excluded acceptance is indicated by the hatched areas in Fig. 3.

The fitted meson radius parameter, common to all the resonances in the fit, is found to be in very good agreement with the value used in the simulation. The dikaon mass resolutions analytically included in the relativistic Breit–Wigner model are found to be consistent with the nominal resolutions derived from the direct study of the $B_s^0 \rightarrow \phi\gamma$ and $B_s^0 \rightarrow f_2'(1525)\gamma$ simulated samples. Small biases on the mass and width parameters due to reconstruction and selection effects are measured in the fit to determine the acceptance function,

$$\begin{aligned}\delta\mu_{\phi(1020)}^{\text{sim}} &= \mu_{\phi(1020)}^{\text{fit}} - \mu_{\phi(1020)}^{\text{sim}} &= (0.041 \pm 0.007 \text{ }^{+0.004}_{-0.014}) \text{ MeV}/c^2, \\ \delta\Gamma_{\phi(1020)}^{\text{sim}}/\Gamma_{\phi(1020)}^{\text{sim}} & &= (2.1 \pm 0.5 \pm 0.1)\%, \\ \delta\mu_{f_2'(1525)}^{\text{sim}} & &= (0.3 \pm 0.1 \pm 0.1) \text{ MeV}/c^2, \\ \delta\Gamma_{f_2'(1525)}^{\text{sim}}/\Gamma_{f_2'(1525)}^{\text{sim}} & &= (1.4 \pm 0.3 \text{ }^{+0.2}_{-0.1})\%,\end{aligned}$$

where the first uncertainties are due to the limited statistics of the simulated samples, and the second are systematic uncertainties obtained by varying the acceptance model and the simulation weighting procedures as discussed in Sect. 6.1. These reconstruction biases derived from simulation are used to correct the mass-shape parameters measured in data for the $\phi(1020)$ and the $f_2'(1525)$ resonances.

4.3 Background model

After $s\mathcal{P}$ lot subtraction of the combinatorial background and the partially reconstructed B decays, the background contamination is dominated by the misidentified $B^0 \rightarrow K^+\pi^-\gamma$ and $\Lambda_b^0 \rightarrow pK^-\gamma$ decays which are both expected to contribute at the level of a few percent in the signal region. A small and well localised contribution from $B^0 \rightarrow \bar{D}^0(K^+K^-)\pi^0$ decays with a high-energy neutral pion reconstructed as a photon is also expected. Other peaking contaminations, *e.g.* charmless $K^+K^-\pi^0$, are assumed to be small and therefore neglected in the nominal model. This assumption is addressed in the studies of systematic uncertainties.

The two-dimensional distribution of the $K^+\pi^-\gamma$ contamination in the $(m_{KK}, |\cos\theta_{KK}|)$ observables plane is modelled using a dedicated selection of a reconstructed and identified $K^+\pi^-\gamma$ data sample. The event reconstruction and selection strictly reproduce the requirements discussed in Sect. 2 for the $B_s^0 \rightarrow K^+K^-\gamma$ signal with an adapted exclusive criteria for the $K^+\pi^-$ dihadron identification. The $s\mathcal{P}$ lot technique is used to extract the $B^0 \rightarrow K^+\pi^-\gamma$ contribution, and the dihadron mass and helicity angle are both re-evaluated under the dikaon hypothesis, *i.e.* by assigning a kaon mass to the pion candidate. The same procedure is applied to the baryonic $\Lambda_b^0 \rightarrow pK^-\gamma$ decay, assigning the kaon mass to the proton candidate. In addition to the mass substitution, $m_{\pi^+(p)} \rightarrow m_K$, correction weights derived from simulation are applied to the selected $K^+\pi^-\gamma$ and $pK^-\gamma$ data candidates to ensure their distributions correctly reproduce the corresponding misidentified contamination passing the exclusive dikaon identification requirements. The resulting two-dimensional projections of the 24×10^4 (3×10^4) $K^+\pi^-\gamma$ ($pK^-\gamma$) candidates, displayed in Fig. 4, are used to build the background binned PDFs.

The background-subtracted $K^+K^-\gamma$ sample possibly includes contaminations from high-energy neutral pions misidentified as photons. The peaking $(K\pi^0)^\pm K^\mp$ decay modes are highly suppressed by the anti-charm veto. The poorly known $(K^+K^-)\pi^0$ charmless

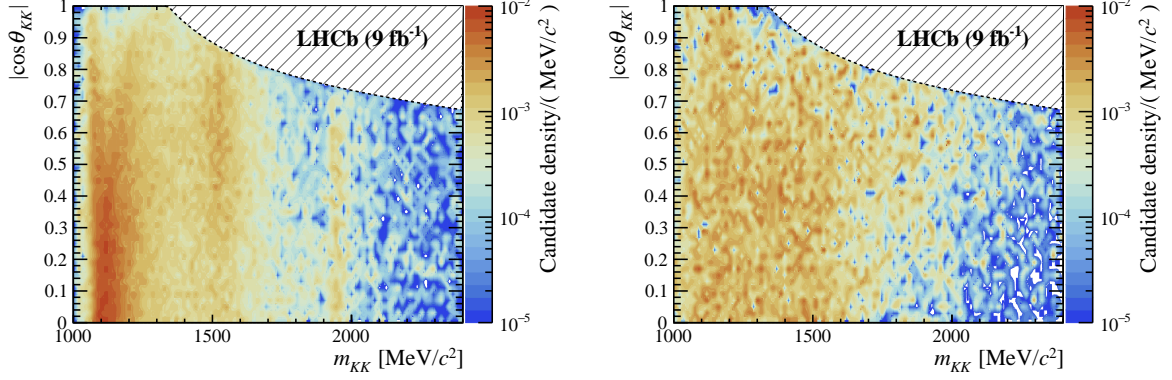


Figure 4: Reconstructed (left) $B^0 \rightarrow K^+\pi^-\gamma$ and (right) $\Lambda_b^0 \rightarrow pK^-\gamma$ candidates, projected on the $(m_{KK}, |\cos\theta_{KK}|)$ plane. The dihadron mass and helicity observables are computed assigning the kaon mass to the pion and proton tracks. The mass-shifted contributions of $K^*(892)^0$, $K_2^*(1430)^0$ and $\bar{D}^0 \rightarrow K^+\pi^-$ are clearly visible in the projection of the $B^0 \rightarrow K^+\pi^-\gamma$ candidates.

contamination is expected to be small and is treated as a source of systematic uncertainty. Other doubly misidentified contamination, for instance from $(K^+\pi^-)\pi^0$, are included in the data-derived description of the $(K^+\pi^-)\gamma$ contamination, discussed above. The suppressed but well-localised contamination from the charmed decay mode $B^0 \rightarrow \bar{D}^0\pi^0$, with a visible branching fraction $\mathcal{B}(B^0 \rightarrow \bar{D}^0\pi^0) \cdot \mathcal{B}(\bar{D}^0 \rightarrow K^+K^-) = (1.07 \pm 0.06) \times 10^{-6}$, further suppressed by the neutral pion misidentification, is included in the amplitude model as an incoherent scalar contribution with a uniform helicity distribution. The $\bar{D}^0 \rightarrow K^+K^-$ mass shape is described as a narrow Gaussian peak with a resolution of about $6.5 \text{ MeV}/c^2$, adjusted to the dikaon mass distribution around the D^0 mass selected in the $K^+K^-\gamma$ upper mass sideband.

5 Amplitude Fit

5.1 Fit procedure and nominal isobar model

An unbinned extended likelihood fit of the nominal model is applied to the *sWeighted* data sample, where the *sWeights* are determined from a mass-fit to the combined Run 1 and Run 2 data. The model is adjusted to data by minimizing the weighted negative log-likelihood function defined as

$$-\ln\mathcal{L}_\omega(\vec{\rho}) = -\sum_i^N \omega_i \ln\mathcal{P}_i(m_{KK}, |\cos\theta_{KK}|; \vec{\rho}), \quad (31)$$

where $\mathcal{P}_i(m_{KK}, |\cos\theta_{KK}|; \vec{\rho})$ is the model PDF evaluated for the i^{th} event observables given the set of parameters $\vec{\rho}$, and ω_i is the event weight derived from the *sPlot* formalism. The PDF defined in Eq. 25 is applied to the whole data sample, combining Run 1 and Run 2 candidates, using the weighted average acceptance

$$\varepsilon(m_{KK}, |\cos\theta_{KK}|) = f_1 \times \varepsilon_{\text{Run1}}(m_{KK}, |\cos\theta_{KK}|) + (1 - f_1) \times \varepsilon_{\text{Run2}}(m_{KK}, |\cos\theta_{KK}|), \quad (32)$$

Table 1: Selected states contributing to the baseline isobar model. The nominal mass and width parameters used to model the resonant lineshapes are reported in the 3rd and 4th column [11] ([42]^(*)). When not specifically measured, the branching fraction to the K^+K^- final state (5th column) is taken as half of the $\mathcal{B}_{K\bar{K}}$ decay rate, neglecting any phase space effect for the heavy states far from the kinematic threshold. The last three columns indicate the measured isobar coefficients, $|c_R|$, the corresponding squared significance, $\chi_{|c_R|}^2$, and the increase in negative log-likelihood when the state is removed from the baseline model, $\Delta\ln\mathcal{L}$.

State	J^{PC}	μ_R [MeV/ c^2]	Γ_R [MeV/ c^2]	$\mathcal{B}_{K^+K^-}$ [%]	$ c_R $ [$\times 10$]	$\chi_{ c_R }^2$	$\Delta\ln\mathcal{L}$
$\phi(1020)$	1^{--}	1019.461 ± 0.016	4.249 ± 0.013	49.2 ± 0.5	10 (fix)	-	-
$f'_2(1525)$	2^{++}	1517.4 ± 2.5	86 ± 5	43.8 ± 1.1	4.16 ± 0.09	2270	-
$\phi(1680)$	1^{--}	1689 ± 12 ^(*)	211 ± 24 ^(*)	seen	2.40 ± 0.15	266	+304
$f_2(1270)$	2^{++}	1275.5 ± 0.8	$186.6^{+2.2}_{-2.5}$	$2.30^{+0.25}_{-0.20}$	1.07 ± 0.17	41	+18
$\phi_3(1850)$	3^{--}	1854 ± 7	87^{+28}_{-23}	seen	0.61 ± 0.16	14	+15
$f_2(2010)$	2^{++}	2011^{+62}_{-76}	202^{+67}_{-62}	seen	0.74 ± 0.18	16	+13
$(KK)_{NR}$	1^{--}	-	-	-	0.79 ± 0.26	10	+17

where f_1 is the relative Run 1 signal yield normalized to the integrated acceptance ratio.

As the signal PDF normalisation is related to the yield parameter \mathcal{N}_s , one reference isobar contribution and its phase can be fixed by setting to unity the complex coefficient associated to the $\phi(1020)$ meson, $c_{\phi(1020)} = (1, 0)$. In the assumed limit of no B_s^0/\bar{B}_s^0 asymmetry, a reference phase can also be fixed for the incoherent even-spin subsystem. This is done by setting the phase of the $f'_2(1525)$ amplitude factor to zero. With this convention, the even-spin complex phase is measured relative to the $f'_2(1525)$ state, and the phase of the odd-spin components is relative to the $\phi(1020)$ resonance.

The isobar model for the signal amplitude is built by selecting the possible contributions among the well-established unflavored isoscalar mesons that have been observed in the dikaon final state [11]. Each candidate is accepted in the nominal model if it significantly improves the fit quality. Namely, the negative log-likelihood minimum is required to increase by more than $\Delta\ln\mathcal{L} = 12.5$ units when the state is removed from the model, roughly indicating a $\sqrt{2\Delta\ln\mathcal{L}} = 5$ standard deviations (σ) effect.⁴ In addition, the squared significance of the fitted isobar coefficient, $\chi_{|c_R|}^2 = |c_R/\sigma_{c_R}|^2$, is required to exceed nine units to avoid selecting a poorly resolved amplitude that mostly improves the fit quality through its contribution to the interference pattern. The selected states passing those criteria are summarized in Table 1, together with their statistical significances and the world average masses and widths used to parameterise their amplitude description. The free lineshape parameters for the $\phi(1020)$ and $f'_2(1525)$ mesons are found to be consistent with the current measurements, and the $\phi(1020)$ meson radius is measured as $r_\phi = 1.01 \pm 0.13$ (GeV/ c)⁻¹.

Besides the dominant contributions from the $\phi(1020)$ and the $f'_2(1525)$ mesons, the fit indicates a high-significance contribution from the $(s\bar{s})$ -dominated vector meson, $\phi(1680)$,

⁴To better reflect their statistical interpretation, the quoted likelihood variations throughout the text implicitly include the global scaling factor $\alpha = \frac{\sum_i^N \omega_i}{\sum_i^N \omega_i^2}$ that aims at accounting for the statistical dilution due to the $s\mathcal{P}$ lot signal weights such that $\Delta\ln\mathcal{L} = \alpha\Delta\ln\mathcal{L}_\omega$. The scale factor measured on the selected sample is $\alpha = 0.67$.

with a fit fraction relative to the $\phi(1020)$ of the order of 6%. The $f_2(1270)$ state, the isoscalar partner of the $f_2'(1525)$ tensor meson, is found to contribute at the level of 1% to the overall amplitude, and the $J^{PC} = 3^{--} s\bar{s}$ candidate, $\phi_3(1850)$, is measured with a relative fit fraction of the order of 0.3%. The amplitude fit also indicates a possible contribution from a heavy tensor state around 2 GeV/ c^2 . Several separate candidates are listed in Ref. [11] in that mass region, $f_2(1910)$, $f_2(1950)$, $f_2(2010)$ or $f_2(2150)$, which all contribute with a similar significance. The $f_2(2010)$ state is slightly preferred by the fit, and is retained.

The nominal model includes a nonresonant component, $(\text{KK})_{\text{NR}}$, modelled as a pure P-wave uniformly distributed in mass with a constant phase: $\mathcal{A}_{\text{NR}}(m_{KK}, \theta_{KK}) = d_{10}^1(\theta_{KK})$. The nonresonant amplitude is found to contribute at the level of 0.5% with a statistical significance of $\Delta \ln \mathcal{L} = +17$. This contribution is, however, weakly resolved, and its significance is strongly correlated to the parameterisation of the other vector components. In particular, the significance of the nonresonant amplitude decreases either when the $\phi(1680)$ state width parameter increases, or when the relativistic tail of the $\phi(1020)$ meson increases at a low radius value.

The nominal PDF model depends on twenty free parameters: four overall normalisation yields, \mathcal{N}_s , \mathcal{N}_{B^0} , $\mathcal{N}_{\Lambda_b^0}$ and \mathcal{N}_{D^0} , parameterising the signal and backgrounds contributions to the data, six relative isobar factors $|c_{\text{R}}|$, their five relative phases δ_{R} , the mass and width parameters of the dominant resonances, $\phi(1020)$ and $f_2'(1525)$, as well as the Blatt–Weisskopf radius parameter of the former. The Breit–Wigner parameters of other resonant states are fixed to the world average values reported in Table 1. The corresponding fit model projected on the mass and helicity observables, m_{KK} and $|\cos \theta_{KK}|$, is shown in Fig. 5. The fitted $B_s^0 \rightarrow K^+ K^- \gamma$ signal yield is found to be $\mathcal{N}_s = (44.4 \pm 0.4) \times 10^3$. The fitted contamination of the misidentified backgrounds $B^0 \rightarrow K^+ \pi^- \gamma$ and $\Lambda_b^0 \rightarrow p K^- \gamma$ are $6.3 \pm 0.7\%$ and $5.4 \pm 0.9\%$, respectively, in good agreement with the expectations derived from simulation studies discussed in Sect. 2. The residual background yield from the suppressed $B^0 \rightarrow \bar{D}^0(K^+ K^-) \pi^0$ decay is found to be $\mathcal{N}_{D^0} < 110$, with 95% confidence.

The individual contribution of each component R to the $B_s^0 \rightarrow K^+ K^- \gamma$ amplitude model is measured by defining the fit fractions in the analysis mass range $m_{KK} \in [2m_K, 2400] \text{ MeV}/c^2$ as

$$\mathcal{F}_{\text{R}} = |c_{\text{R}}|^2 \frac{\int_0^{+1} \int_{2m_K}^{2.4 \text{ GeV}/c^2} |\mathcal{A}_{\text{R}}(m_{KK}, |\cos \theta_{KK}|)|^2 d\phi_3}{\int_0^{+1} \int_{2m_K}^{2.4 \text{ GeV}/c^2} \sum_{\text{P}} \left| \sum_{\text{R}_p} c_{\text{R}_p} \cdot \mathcal{A}_{\text{R}_p}(m_{KK}, |\cos \theta_{KK}|) \right|^2 d\phi_3}, \quad (33)$$

where $d\phi_3 = \mathcal{J}_3(m_{KK}) dm_{KK} d\cos \theta_{KK}$ is the phase space volume. Although it is not required by the minimization process, each individual amplitude of the isobar model is normalised to unity,

$$\int_0^{+1} \int_{2m_K}^{2.4 \text{ GeV}/c^2} |\mathcal{A}_{\text{R}_p}(m_{KK}, |\cos \theta_{KK}|)|^2 d\phi_3 = 1, \quad (34)$$

to allow an easier interpretation of the associated isobar factor that directly provides the relative fit fractions normalized to $\phi(1020)$: $\mathcal{F}_{\text{R}}/\mathcal{F}_{\phi(1020)} = |c_{\text{R}}|^2$.

To account for the statistical dilution due to the $s\mathcal{P}$ lot weights, the asymptotically correct approach [43, 44] is adopted to evaluate the statistical error on the fit parameters

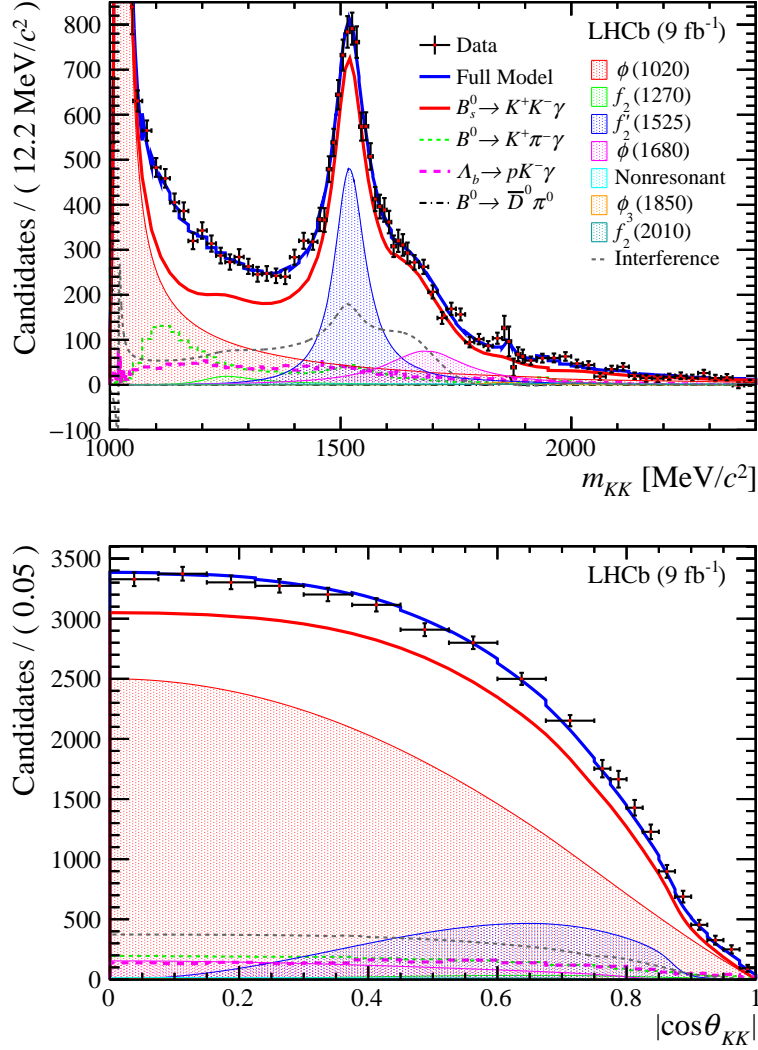


Figure 5: One-dimensional projection of the nominal fit on (top) m_{KK} and (bottom) $|\cos\theta_{KK}|$ observables. Nonuniform binning is applied on both projections, with the bin width varying from 0.5 MeV/ c^2 (in the $\phi(1020)$ region) to 20 MeV/ c^2 for m_{KK} , and from 0.025 to 0.075 for $|\cos\theta_{KK}|$.

and on the derived fit fractions. The statistical coverage of the method is validated using a large sample of pseudoexperiments. For that purpose, a three-dimensional binned PDF representation of the data sample observables ($m_{KK\gamma}$, m_{KK} , $|\cos\theta_{KK}|$) is prepared using an adaptative binning adjusted to the data density. Pseudodata samples are randomly generated from that PDF with a random yield consistent with the size of the selected data sample. Each step of the analysis, including evaluating the $sWeights$, is applied to the generated pseudoexperiments. As an illustration, the pseudodata dispersion of the $f_2'(1525)$ relative fit fraction, $\mathcal{F}_{f_2'(1525)}/\mathcal{F}_{\phi(1020)}$, compared with the statistical uncertainty derived from the fit using the asymptotically correct estimation of the parameters' covariance, is displayed in Fig. 6. The statistical interval corresponding to 68.3% of the pseudodata population on both sides of the distribution maximum is found to be almost symmetrical and in good agreement with the asymptotic error interval obtained from the fit to data.

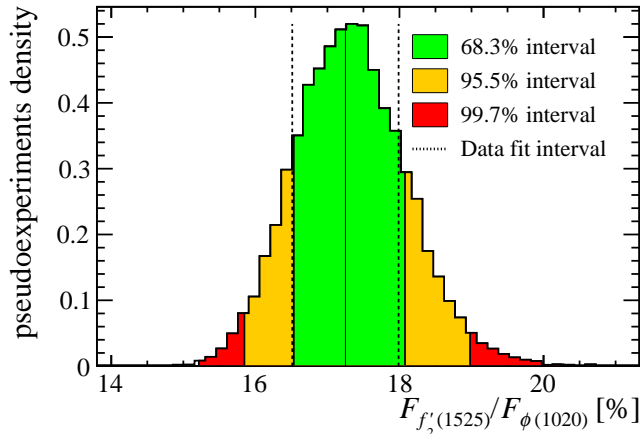


Figure 6: Distribution from pseudoexperiments of the $f'_2(1525)$ relative fit fraction normalized to the $\phi(1020)$ fraction. The one, two and three σ asymmetric intervals, containing respectively 68.3%, 95.5% and 99.7% of the pseudodata population on both sides of the distribution mean, are indicated by the green, orange and red coloured areas, respectively. The solid and dotted vertical lines indicate the central value and the statistical interval returned by the fit to the data sample, evaluated using an asymptotically correct approach.

5.2 Likelihood minima pattern

Several distinct and almost degenerate $-\ln\mathcal{L}$ minima separated by less than three units are found by exploring the isobar parameter space. This quasi-degenerated behaviour can be explained by the poorly constrained interference pattern in the symmetrical $B_s^0 \rightarrow K^+ K^- \gamma$ decay where the odd- and even-spin components form two incoherent amplitude systems.

The even-spin subsystem consists of a largely dominant $f'_2(1525)$ amplitude surrounded by the two small $f_2(1270)$ and $f_2(2010)$ contributions that may either interfere constructively or destructively with almost the same statistical significance. A first set of four solutions separated by less than one log-likelihood unit, hereafter denoted X_i with $i \in \{0, 1, 2, 3\}$, originate from the interference ambiguities in the even-spin subsystem, leaving the structure of the odd-spin system unchanged. The overall minimum solution X_0 ($\Delta\ln\mathcal{L} = 0$) illustrated in Fig. 5 corresponds to the smallest fit fractions for each resonant state, along with positive interference. Other solutions with a larger amplitude and destructive interference, either for the $f_2(2010)$ (X_1 , $\Delta\ln\mathcal{L} = 0.1$) or the $f_2(1270)$ (X_2 , $\Delta\ln\mathcal{L} = 0.5$) or both (X_3 , $\Delta\ln\mathcal{L} = 0.6$), are barely disfavoured. The overall contribution of the three spin-2 states, including their interference, is found to be 16.8% identically for the four solutions X_i that only differ by their internal interference pattern. The dominant contribution of the $f'_2(1525)$ state varies from 12% with constructive interference for the preferred solution X_0 , to 20% with negative interference for the solution X_3 .

A similar ambiguity appears in the odd-spin system, which consists of the two well-separated vector resonances, $\phi(1020)$ and $\phi(1680)$, connected by the small nonresonant P-wave, $(KK)_{\text{NR}}$, that can either interfere constructively or destructively in the $\phi(1680)$ region. As a consequence, another set of four minima, denoted by Y_i with $i \in \{0, 1, 2, 3\}$, is obtained. It approximately replicates the X_i solutions for the even-spin subsystem and exhibits an alternative interference pattern for the vector components with a large $\phi(1680)$ fit fraction of about 18% along with large destructive interference, to be compared to

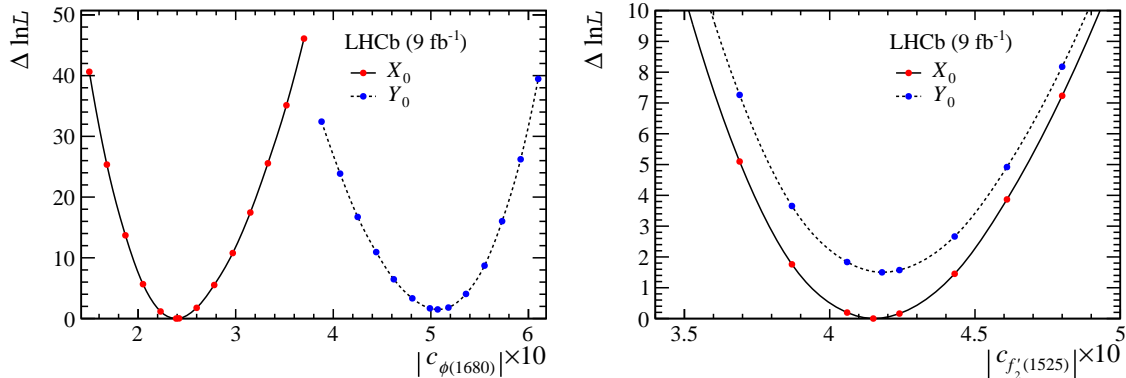


Figure 7: Negative log-likelihood scans as a function of (left) the vector isobar $|c_{\phi(1680)}|$ and (right) the tensor isobar $|c_{f'_2(1525)}|$ in the vicinity of the fit solutions X_0 and Y_0 . The fit minima, well separated in the vector system, correspond to the same location in the tensor system.

4% with constructive interference for the solutions set X_i . The small spin-3 amplitude, $\phi_3(1850)$, does not induce any additional minimum pattern in the odd sector as its interference vanishes in the integration over the helicity observable due to the orthogonality of the Wigner d-functions. The four Y_i solutions are modestly disfavored with a log-likelihood shift from $\Delta \ln \mathcal{L} = 1.5$ to 2.9 units. The even-spin structure of each Y_i solution is very close to that of the corresponding X_i one, with a consistent overall tensor fraction identical for the four solutions within 0.1%. For illustration, the likelihood scans of the $\phi(1680)$ and the $f'_2(1525)$ isobars in the vicinity of the solutions X_0 and Y_0 are compared in Fig. 7. The detailed amplitude structure of the eight quasi-degenerated solutions is summarized in Appendix A.

The very large $\phi(1680)$ fit fraction of the Y_i solutions is questionable, as this radial excitation of the ground state is expected to mainly decay into $\bar{K}^{*0}K$ and $\phi\eta$ final states [11, 45]. The small partial decay rates of the $\phi(1680)$ to a kaon pair [46, 47] disfavors a large contribution to the $(K^+K^-)\gamma$ final state. The solutions Y_i would imply an unlikely large $B_s^0 \rightarrow \phi(1680)\gamma$ branching fraction ratio

$$R_{\phi\gamma} = \frac{\mathcal{B}(B_s^0 \rightarrow \phi(1680)\gamma)}{\mathcal{B}(B_s^0 \rightarrow \phi(1020)\gamma)} \simeq 5.5 \pm 0.9.$$

This presumption is also supported by the amplitude analysis of the $B_s^0 \rightarrow J/\psi K^+ K^-$ decay [48] which reports the fit fraction $\mathcal{F}_{\phi(1680)}^{J/\psi K^+ K^-} = 4.0 \pm 0.3$ (stat.) ± 0.3 (syst.)%, very consistent with the value observed for the fit solutions X_i .

Similar arguments can be made for the orbitally excited tensor $f'_2(1525)$ and its almost decoupled isoscalar partner, $f_2(1270)$. The large $f_2(1270)$ fit fraction of the fit solutions X_2 and X_3 (or equivalently Y_2 and Y_3) would imply the unlikely large ratio of branching fractions

$$R_{f_2\gamma} = \frac{\mathcal{B}(B_s^0 \rightarrow f_2(1270)\gamma)}{\mathcal{B}(B_s^0 \rightarrow f'_2(1525)\gamma)} = 3.0 \pm 0.3.$$

Although most of the quasi-degenerate fit solutions are disfavoured by external arguments, no definitive statement can be derived from the amplitude fit to the current data, given the numerical proximity of the negative log-likelihood minima. It is worth noting, however, that the tensor subsystem including the three states $f_2 = \{f_2(1270), f'_2(1525), f_2(2010)\}$

is found to contribute with an overall fit fraction of about 17.0% consistently for all the eight solutions. The $\phi(1020)$ and $f_2'(1525)$ lineshape parameters as well as the signal and background composition of the data sample are also found to be independent of the amplitude fit solutions.

6 Systematic uncertainties

The sources of systematic uncertainty can be organised into four main categories driven by the analysis steps: the uncertainties related to the $K^+K^-\gamma$ mass fit and the determination of the $s\mathcal{P}$ lot weights, the uncertainties related to the parametrisation of the two-dimensional acceptance, the uncertainties related to the amplitude PDF and the description of the backgrounds, and the uncertainties related to the nominal choices for the dikaon isobar model.

The systematic uncertainties are summarised in Table 2, and details are provided in the following subsections. The systematic uncertainties are presented as determined for the best-fit minimum, but their values are similar for other solutions.

6.1 Mass fit and $s\mathcal{P}$ lot weights.

The combinatorial $K^+K^-\gamma$ background and the partially reconstructed decays are statistically subtracted by applying $s\mathcal{P}$ lot weights derived from a fit to the reconstructed invariant mass, $m_{KK\gamma}$. The associated uncertainties reported in the third column of Table 2 are obtained by repeating the full amplitude analysis with alternative mass models to extract the $s\mathcal{P}$ lot weights. The fixed parameters that describe the tails on both sides of the signal peak have been varied and an alternative shape for the combinatorial background has been tested. Particular attention was paid to the modelling of the partially reconstructed backgrounds that extend into the signal mass region. The fixed parameters of the one-missing-pion shape have been varied by several times their uncertainty as derived from simulation studies. Similar variations have been applied to the low-mass two-missing-pion component that slightly overlaps with the signal peak. Additionally, the fit has been repeated in the reduced mass range, $m_{KK\gamma} \in [5100, 6400] \text{ MeV}/c^2$, with this low-mass component removed from the fit model. To further check that the partially reconstructed background components are correctly subtracted in the signal mass region, the full data sample has been split into four bins of the dikaon mass, with very different levels of contamination: the $\phi(1020)$ region, $m_{KK} \in [1000, 1100] \text{ MeV}/c^2$, which is almost background free, the two intermediate regions $m_{KK} \in [1100, 1300] \text{ MeV}/c^2$ and $m_{KK} \in [1300, 1525] \text{ MeV}/c^2$, where most of the partially reconstructed backgrounds accumulate, and the high dikaon mass region $m_{KK} \in [1525, 2400] \text{ MeV}/c^2$. A limited variation of the amplitude fit fractions is obtained when applying $s\mathcal{W}$ eights extracted in separate m_{KK} bins. The same procedure is applied to the helicity observable, splitting the data sample into four bins of $|\cos\theta_{KK}|$ almost equally populated. The difference in the $m_{KK\gamma}$ mass distribution over time has also been tested by splitting the data sample into data-taking periods. A small change in the amplitude fit results is obtained when extracting the $s\mathcal{W}$ eights from separate mass fits per year of data taking or when splitting the data into two subsamples for Run 1 and Run 2. A simultaneous amplitude fit to the Run 1 and Run 2 data with separate acceptances and independent background contributions has alternatively been performed.

Table 2: Systematic uncertainties on the parameters of the amplitude fit: fit fractions, \mathcal{F}_R , relative fit fractions, $\mathcal{F}_R/\mathcal{F}_\phi$, isobar phases, δ_R , and mass-shape parameters, μ_R , Γ_R and r_ϕ . The uncertainties due to the mass fit and the $s\mathcal{P}$ lot weights, the two-dimensional acceptance definition, the amplitude fit PDF and the isobar model are given from the 3rd to the 6th columns, respectively. The last column shows the overall uncertainties calculated as the quadratic sum of the individual sources.

		$m_{KK\gamma}$ fit	Acceptance	Amp. fit	Isobar model	Total
$\phi(1020)$	\mathcal{F}_R [%]	(+0.2) (-0.7)	(+0.9) (-0.4)	(+0.3) (-0.9)	(+0.3) (-0.5)	(+1.0) (-1.2)
	μ_R [keV/c ²]	(+5) (-6)	(+5) (-6)	(+5) (-4)	(+6) (-14)	(+11) (-16)
	Γ_R [keV/c ²]	(+3) (-10)	(+8) (-7)	(+14) (-62)	(+20) (-82)	(+26) (-103)
	r_ϕ [(GeV/c) ⁻¹]	(+0.02) (-0.07)	(+0.05) (-0.04)	(+0.05) (-0.06)	± 0.09	± 0.12
$f_2(1270)$	\mathcal{F}_R [%]	(+0.09) (-0.22)	(+0.04) (-0.07)	(+0.13) (-0.21)	(+0.09) (-0.13)	(+0.2) (-0.3)
	$\mathcal{F}_R/\mathcal{F}_\phi$ [%]	(+0.13) (-0.31)	(+0.05) (-0.10)	(+0.2) (-0.3)	(+0.13) (-0.19)	(+0.3) (-0.5)
	δ_R [deg.]	(+6.3) (-3.8)	(+1.1) (-0.9)	(+5.6) (-8.5)	(+23.1) (-14.1)	(+24.6) (-16.9)
$f'_2(1525)$	\mathcal{F}_R [%]	(+0.3) (-0.2)	(+0.2) (-0.1)	(+0.6) (-0.3)	(+0.6) (-0.2)	(+0.9) (-0.4)
	$\mathcal{F}_R/\mathcal{F}_\phi$ [%]	(+0.3) (-0.1)	(+0.3) (-0.4)	(+0.9) (-0.2)	(+0.9) (-0.2)	(+1.3) (-0.5)
	μ_R [MeV/c ²]	(+0.3) (-0.8)	± 0.2	(+0.6) (-0.5)	(+1.2) (-1.7)	(+1.4) (-1.9)
	Γ_R [MeV/c ²]	(+0.6) (-0.9)	(+0.8) (-0.4)	(+2.0) (-0.6)	(+2.5) (-1.0)	(+3.4) (-1.5)
$\phi(1680)$	\mathcal{F}_R [%]	(+0.3) (-0.5)	± 0.2	± 0.3	± 0.5	± 0.7
	$\mathcal{F}_R/\mathcal{F}_\phi$ [%]	(+0.4) (-0.6)	(+0.3) (-0.3)	(+0.5) (-0.4)	± 0.7	(+1.0) (-1.1)
	δ_R [deg.]	(+2.7) (-3.1)	(+1.2) (-1.4)	(+3.9) (-1.7)	(+6.7) (-6.9)	(+8.3) (-7.9)
$\phi_3(1850)$	\mathcal{F}_R [%]	(+0.13) (-0.07)	± 0.03	(+0.07) (-0.04)	(+0.12) (-0.10)	(+0.19) (-0.13)
	$\mathcal{F}_R/\mathcal{F}_\phi$ [%]	(+0.19) (-0.10)	(+0.05) (-0.04)	(+0.10) (-0.06)	(+0.17) (-0.14)	(+0.3) (-0.2)
	δ_R [deg.]	(+1.4) (-4.7)	(+2.7) (-1.5)	(+4.1) (-3.2)	(+11.5) (-10.5)	(+12.6) (-12.1)
$f_2(2010)$	\mathcal{F}_R [%]	(+0.08) (-0.01)	(+0.02) (-0.07)	(+0.14) (-0.07)	(+0.11) (-0.10)	(+0.20) (-0.14)
	$\mathcal{F}_R/\mathcal{F}_\phi$ [%]	(+0.11) (-0.01)	(+0.02) (-0.10)	(+0.21) (-0.10)	(+0.16) (-0.14)	(+0.3) (-0.2)
	δ_R [deg.]	(+17.1) (-15.9)	(+9.1) (-2.8)	(+20.5) (-11.7)	(+43.7) (-55.1)	(+52.1) (-58.6)
(KK) _{NR}	\mathcal{F}_R [%]	(+0.21) (-0.08)	(+0.04) (-0.14)	(+0.23) (-0.12)	(+0.12) (-0.09)	(+0.3) (-0.2)
	$\mathcal{F}_R/\mathcal{F}_\phi$ [%]	(+0.31) (-0.11)	(+0.07) (-0.21)	(+0.34) (-0.17)	(+0.17) (-0.12)	(+0.5) (-0.3)
	δ_R [deg.]	(+1.9) (-4.5)	(+1.7) (-2.8)	(+6.1) (-6.7)	(+5.5) (-3.9)	(+8.5) (-9.4)

The small difference with the nominal strategy is included in the budget of systematic uncertainties.

6.2 Acceptance model

The acceptance-related uncertainties reported in the fourth column of Table 2 address the acceptance model definition, the simulation corrections weights and the limited data samples used to derive the acceptance function. The robustness of the acceptance model has been tested against the choice of the considered simulated decays and using alternative parameterisations. The impact of the limited statistics has been evaluated by repeating the amplitude analysis with sets of acceptance parameters randomly generated according to their covariance. The uncertainties affecting the weights reproducing the dikaon and the photon identification efficiencies [29, 30] have been propagated to the acceptance estimate. Alternative weighting corrections [49] have been tested for the kinematics distributions.

6.3 Amplitude PDF and residual backgrounds

The signal PDF defined in Eq. 24 explicitly assumes an equal decay rate for B_s^0 and \bar{B}_s^0 mesons. To check this assumption and the resulting interference cancellation, the amplitude fit is repeated in the unfolded $(m_{KK}, \cos\theta_{KK})$ plane with an adapted PDF for the signal component

$$\mathcal{P}_s(m_{KK}, \theta_{KK}) = \mathcal{N}_s \left[\frac{1-a}{2} \times \mathcal{P}_{B_s^0} + \frac{1+a}{2} \times \mathcal{P}_{\bar{B}_s^0} \right], \quad (35)$$

allowing the asymmetry parameter, a , to vary freely. The measured helicity observable, θ_{KK} , arbitrarily defined with respect to the direction of the positively charged kaon, leads to the flavour-dependent PDF definitions

$$\mathcal{P}_{B_s^0}(m_{KK}, \theta_{KK}) = \varepsilon(m_{KK}, \theta_{KK}) \cdot \mathcal{J}_3(m_{KK}) \cdot \left| \sum_{\text{R}} c_{\text{R}} \cdot \mathcal{A}_{\text{R}}(m_{KK}, \theta_{KK}) \right|^2, \quad (36)$$

$$\mathcal{P}_{\bar{B}_s^0}(m_{KK}, \theta_{KK}) = \mathcal{P}_{B_s^0}(m_{KK}, \pi - \theta_{KK}), \quad (37)$$

where the coherent sum is over all contributions, regardless of their spin parity. In addition, the reference phase for the even-spin states, which is fixed to 0 for the $f_2'(1525)$ in the nominal fit, is allowed to vary to account for the non-exact cancellation of the interference between odd and even spin resonances. The decay asymmetry and the $f_2'(1525)$ relative phase are found to be consistent with no asymmetry within two standard deviations

$$a = (-3.9 \pm 2.2) \times 10^{-2},$$

$$\delta_{f_2'(1525)} = -46 \pm 37 \text{ deg.}$$

The observed variations of the fit parameters that do not exceed 0.3% for the fit fractions are added to the budget of the systematic uncertainties.

A small impact on the amplitude fit is observed when varying the PDFs that describe the background contributions discussed in Sect. 4.3. The possible peaking contribution from charmless $B \rightarrow K^+K^-\pi^0$ decays with a high-energy neutral pion misidentified as $K^+K^-\gamma$ is neglected in the nominal PDF. The expected contamination, roughly

estimated at the level of 0.5% from simulations, is affected by large uncertainties as the actual resonant structure of this final state is poorly known. The final state most similar to the signal, $B_s^0 \rightarrow \phi\pi^0$, has a predicted branching fraction of $\mathcal{O}(10^{-7})$, leading to an expected negligible contamination of $\mathcal{O}(0.1\%)$. The same final state in the B^0 decay is expected to be further suppressed, $\mathcal{O}(10^{-9})$, and constrained by the upper limit [50] provided by Belle of $\mathcal{B}(B^0 \rightarrow \phi\pi^0) < 1.5 \times 10^{-7}$. Evidence at 3.5σ for the $B^0 \rightarrow K^+K^-\pi^0$ decay was reported by Belle [51], with a relatively large branching fraction of $\mathcal{B} = (2.17 \pm 0.60 \pm 0.24) \times 10^{-6}$. The charged intermediate states, $K^{*\pm}K^\mp$, are removed from the analysis by the anti-charm veto. However, the unknown S-wave $(K^+K^-)\pi^0$ contribution might contaminate the $(K^+K^-)\gamma$ signal at the level of $\mathcal{O}(1\%)$. No clear statement about a possible intermediate (K^+K^-) structure could be made with the Belle data, however, BaBar has reported [52] a possible observation of a broad structure peaking near $m_{KK} \sim 1500 \text{ MeV}/c^2$ in the corresponding charged decay, $B^+ \rightarrow K^+K^-\pi^+$. LHCb has performed the first amplitude analysis of this three-body charged mode [53], and a good description of the data pattern in that mass region is also observed when including the contribution of a vector resonance compatible with the $\rho(1450)$ hypothesis.

The potentially neglected contamination from the charmless $K^+K^-\pi^0$ decays, which may also include a residual contribution from $K^+K^-\eta(\rightarrow\gamma\gamma)$ decays not fully accounted for in the partially reconstructed backgrounds, has been investigated by adding an incoherent S-wave contribution to the dikaon amplitude. Several possible models have been tested: a resonant S-wave contribution based on the scalar mesons $f_0(980)\pi^0$ or $f_0(1500)\pi^0$, a resonant vector-scalar contribution based on $\phi(1020)\pi^0$ or $\rho^0(1450)\pi^0$, a resonant tensor-scalar contribution based on $f_2'(1525)\pi^0$, and a nonresonant scalar contributions $(K^+K^-)_{\text{NR}}\pi^0$. The corresponding PDFs are built assuming the same acceptance as for the $K^+K^-\gamma$ final state. A relativistic Breit–Wigner lineshape is used to describe the $f_0(1500)$ and the $\rho(1450)$ resonances with their world average mass and width [11]. A Flatté lineshape is used for the $f_0(980)$ resonance with the BES parameterisation [54]. The angular dependencies are described by the relevant Wigner d-functions, d_{00}^1 (d_{00}^2) for the vector (tensor) resonances and $d_{00}^0 = 1$ for the scalar hypothesis. Among the different investigated models, the largest contributions are obtained with the $f_0(980)\pi^0$ hypothesis, $\mathcal{N}_{f_0\pi^0}/\mathcal{N}_s = 5.1 \pm 1.0 \%$, and with the $\phi(1020)\pi^0$ hypothesis, $\mathcal{N}_{\phi\pi^0}/\mathcal{N}_s = 1.2 \pm 0.2 \%$, improving the fit quality in both cases. The other considered scalar, vector or tensor contributions around $1.5 \text{ GeV}/c^2$, $f_0(1500)$, $\rho(1450)$ or $f_2'(1525)$, as well as the nonresonant S-wave hypothesis, are all found to vanish in the fit. The possibly significant $K^+K^-\pi^0$ contamination at low m_{KK} mass, much larger than expected in particular for the very suppressed $\phi\pi^0$ final state hypothesis, may indicate an opportunistic improvement of the fit when adding these additional degrees of freedom. Systematic uncertainties are conservatively derived from the largest observed positive and negative variations of each isobar parameter when adding any of the above $K^+K^-\pi^0$ hypotheses to the fit model.

6.4 Isobar model

The lineshape parameters are fixed to their world average measurements for the $f_2(1270)$, $\phi(1680)$, $\phi_3(1850)$ and $f_2(2010)$ components of the nominal isobar model, while they are free to vary for the two dominant $\phi(1020)$ and $f_2'(1525)$ resonances. The amplitude fit has been repeated by varying each fixed parameter within its uncertainty range by $\pm 1\sigma$. The quadratic sum of the parameter variations, limited to few 0.1% at most for the fit

fractions, are added to the systematic uncertainty. When allowed to vary freely, the lineshape parameters for the subdominant $\phi(1680)$ component are found to be

$$\begin{aligned}\mu_{\phi(1680)} &= 1688 \pm 10 \text{ (stat.) MeV}/c^2, \\ \Gamma_{\phi(1680)} &= 264 \pm 28 \text{ (stat.) MeV}/c^2,\end{aligned}$$

in good agreement with the nominal value taken from the Belle measurement [42] and consistent with the current world average estimate [11]. Moreover, the statistical significance of the isobar coefficient for the nonresonant $(\text{KK})_{\text{NR}}$ and for the $\phi_3(1850)$ components are both reduced below the 3σ level with fit fractions measured as $\mathcal{F}_{(\text{KK})_{\text{NR}}} = (0.34 \pm 0.27)\%$ and $\mathcal{F}_{\phi_3(1850)} = (0.15 \pm 0.11)\%$, respectively.

A negligible impact on the fit fractions is observed when varying the nominal $\phi(1020)$ mass resolution, analytically included in the relativistic Breit–Wigner lineshape. Similarly, for higher mass resonances, the resolution has been varied by $\pm 50\%$ of the nominal value, inducing marginal variation on the amplitude fit parameters other than the free $f'_2(1525)$ width that varies accordingly.

The angular momentum in the radiative B decay to a J_{R} -spin state can take $L_B = \{J_{\text{R}} - 1, J_{\text{R}}, J_{\text{R}} + 1\}$ values. The amplitude fit is performed using the lowest value $J_{\text{R}} - 1$ for all resonances. Repeating the fit by fixing the L_B parameter to the other allowed eigenvalues leads to a negligible effect on the fit fractions.

The meson radius that defines the centrifugal correction in the Blatt–Weisskopf form-factors is nominally set in the range $[0.5, 3] \text{ (GeV}/c)^{-1}$ for the light resonances [55]. The $\phi(1020)$ radius parameter r_ϕ is left free to vary in the nominal fit, leading to a measured value of $r_\phi = 1.01 \pm 0.13 \text{ (GeV}/c)^{-1}$. The meson radius for heavier resonances is fixed to the nominal value $r_{f_2} = 3.0 \text{ (GeV}/c)^{-1}$. The likelihood scan of this parameter indicates that large radii are preferred with no clear minimum of the negative log-likelihood up to very large unphysical values. Associated systematics are derived from the maximal negative or positive variations of each of the fit parameters in the wide radius range $r_{f_2} \in [2.0, 10] \text{ (GeV}/c)^{-1}$, corresponding to changes of the log-likelihood by $[+0.7, -3.0]$ units with respect to the nominal point.

6.5 Other possible resonant states

The nominal isobar model includes the isoscalar dikaon states that significantly improve the fit quality according to the selection criteria presented in Sect. 5.1. Several possible resonant candidates with poorly measured properties, and sometimes unclear spectroscopic classification, may additionally contribute in the high-mass region. No large contribution is observed when adding any of the known candidates to the nominal model. The most significant rejected candidate is the $f_4(2050)$ state, just below the significance threshold for inclusion. The measured partial rate, $\mathcal{B}(f_4(2050) \rightarrow K\bar{K}) = (0.68^{+0.34}_{-0.18})\%$, indicates that this state would have a negligible contribution to the signal. This spin-4 meson is generally interpreted as an almost decoupled $u\bar{u} + d\bar{d}$ isoscalar state. The yet unconfirmed associated $s\bar{s}$ heavy partner, $f_4(2300)$, induces a rather significant fit quality improvement, $\Delta \ln \mathcal{L} = -10$. The impact on the nominal fit fractions is small, and no additional systematic is included in the error budget.

Assuming $SU(3)_F$ symmetry, the excited dikaon states are reasonably described by a ρ - ω - ϕ model with an almost ideal singlet-octet mixing and can be interpreted as recurrences

of the ρ - ω - ϕ vector ground state. Except for the well measured $f_2(1270)$ isoscalar, the nominal amplitude model only includes $s\bar{s}$ -dominant states. The largest significance, albeit limited, when adding the partially decoupled isovector partner to the isobar model, is observed for the wide and possibly mixed vector states $\rho(1450)$ and $\rho(1700)$ that both increase the fit quality by $\Delta\ln\mathcal{L} \approx -5$. Including those states essentially has the same impact on the fit as the enlargement of the $\phi(1680)$ width discussed above. A limited fit improvement, $\Delta\ln\mathcal{L} \approx -3$ units, is observed as well with the $a_2(1320)$ isovector partner of the orbitally excited $f_2(1270)$ and $f_2'(1525)$ states. Including this resonance only affects the $f_2(1270)$ fit fractions due to its approximate mass and width degeneracy with its isoscalar partner. The measured $f_2(1270)$ fit fraction must be considered as possibly receiving contributions from both the quasi-degenerate isoscalar partners. No impact is observed with the $a_2(1700)$, possible partner of the $f_2(1640)$ and $f_2(1950)$ isoscalars, nor with the $\rho_3(1690)$ associated to the $\phi_3(1850)$ $s\bar{s}$ state. As no clear evidence of contribution is observed for any of the tested additional states, no additional systematic source is included in the error budget.

7 Results and conclusions

An isobar amplitude analysis of the radiative $B_s^0 \rightarrow K^+ K^- \gamma$ decay mode is performed in the mass range $m_{KK} \in [2m_K, 2400]$ MeV/ c^2 . The $\phi(1020)$ vector meson, accounting for almost 70% of the amplitude, dominates the dikaon structure. Considering the resonant contributions of $f_2(1270)$, $f_2'(1525)$ and $f_2(2010)$ states, the overall tensor contribution to the amplitude is measured as

$$\mathcal{F}_{\{f_2\}} = 16.8 \pm 0.5 \text{ (stat)} \pm 0.7 \text{ (syst)}\%,$$

mostly dominated by the $f_2'(1525)$ state. Several almost statistically equivalent solutions are obtained for the detailed resonant structure depending on whether the low contributing resonances interfere destructively or constructively with the dominant amplitudes. The statistically preferred solution corresponds to the lowest values of all the individual fit fractions along with constructive interferences that contribute for 3.5% and 8.1% in the even-spin and odd-spin subsystems, respectively. The corresponding fit fractions are given in Table 3, together with the measured relative phases. The first quoted uncertainties are statistical and correspond to the 68.3% intervals derived from pseudoexperiments and the second uncertainties are the associated systematic uncertainties. The sum of partial fit fractions is less than unity due to the integrated interference. Larger individual fit fractions, up to 20% for the $f_2'(1525)$ state, associated with large destructive interference, cannot be excluded.

The branching fraction $\mathcal{B}(B_s^0 \rightarrow f_2'(1525)\gamma)$ relative to $\mathcal{B}(B_s^0 \rightarrow \phi(1020)\gamma)$ can be derived from the fit fractions ratio as

$$\frac{\mathcal{B}(B_s^0 \rightarrow f_2'(1525)\gamma)}{\mathcal{B}(B_s^0 \rightarrow \phi(1020)\gamma)} = \frac{\mathcal{B}(\phi(1020) \rightarrow K^+ K^-)}{\mathcal{B}(f_2'(1525) \rightarrow K^+ K^-)} \cdot \frac{\mathcal{F}_{f_2'(1525)}}{\mathcal{F}_{\phi(1020)}}. \quad (38)$$

Using the world average measurements reported in Table 1 for the branching fraction of $\phi(1020)$ and $f_2'(1525)$ into $K^+ K^-$, the ratio

$$\frac{\mathcal{B}(B_s^0 \rightarrow f_2'(1525)\gamma)}{\mathcal{B}(B_s^0 \rightarrow \phi(1020)\gamma)} = 0.194_{-0.008}^{+0.009} \text{ (stat.)}_{-0.005}^{+0.014} \text{ (syst.)} \pm 0.005 \text{ (}\mathcal{B}\text{)}$$

Table 3: Absolute and relative fit fractions (in the mass range $m_{KK} \in [2m_K, 2400]$ MeV/ c^2) and the associated isobar phase for the best-fit solution. The first quoted uncertainties are statistical and correspond to the 68.3% intervals derived from pseudoexperiments, while the second are systematic.

State	Fit fraction [%]	Relative fit fraction [%]	Phase [deg.]
$\phi(1020)$	$70.3^{+0.9}_{-1.0} \text{ }^{+1.0}_{-1.2}$	100	0 (fixed)
$f_2(1270)$	$0.8 \pm 0.3 \text{ }^{+0.2}_{-0.3}$	$1.2^{+0.4}_{-0.3} \text{ }^{+0.3}_{-0.5}$	$-55^{+13}_{-17} \text{ }^{+25}_{-17}$
$f'_2(1525)$	$12.1^{+0.6}_{-0.5} \text{ }^{+0.9}_{-0.4}$	$17.3^{+0.8}_{-0.7} \text{ }^{+1.3}_{-0.5}$	0 (fixed)
$\phi(1680)$	$3.8^{+0.6}_{-0.5} \text{ }^{+0.7}_{-0.7}$	$5.4^{+0.9}_{-0.6} \text{ }^{+1.0}_{-1.1}$	$137^{+5}_{-6} \pm 8$
$\phi_3(1850)$	$0.3^{+0.2}_{-0.1} \text{ }^{+0.2}_{-0.1}$	$0.4^{+0.3}_{-0.2} \text{ }^{+0.3}_{-0.2}$	$-61^{+16}_{-13} \text{ }^{+13}_{-12}$
$f_2(2010)$	$0.4 \pm 0.2 \text{ }^{+0.2}_{-0.1}$	$0.6^{+0.3}_{-0.2} \text{ }^{+0.3}_{-0.2}$	$43^{+30}_{-24} \text{ }^{+52}_{-59}$
$(KK)_{\text{NR}}$	$0.5^{+0.4}_{-0.2} \text{ }^{+0.3}_{-0.2}$	$0.6^{+0.5}_{-0.3} \text{ }^{+0.5}_{-0.3}$	$165^{+6}_{-16} \pm 9$

is obtained for the statistically preferred fit solution that corresponds to the smallest value. The last uncertainty is associated with the ratio of measured branching fractions to the K^+K^- final state. This result establishes the first observation of the radiative B_s^0 decay to an orbitally excited meson, $B_s^0 \rightarrow f'_2(1525)\gamma$, and the second radiative transition observed in the B_s^0 sector [2].

A relative branching ratio can similarly be derived for the $f_2(1270)$ tensor partner,

$$\frac{\mathcal{B}(B_s^0 \rightarrow f_2(1270)\gamma)}{\mathcal{B}(B_s^0 \rightarrow \phi(1020)\gamma)} = 0.25^{+0.09}_{-0.07} \text{ (stat.)}^{+0.06}_{-0.10} \text{ (syst.)} \pm 0.03 \text{ (}\mathcal{B}\text{)},$$

which possibly includes the contribution from its quasi-degenerate isovector partner, $a_2(1320)$. The relative branching fraction of the $\phi(1680) \rightarrow K^+K^-$ contribution is measured as

$$\frac{\mathcal{B}(B_s^0 \rightarrow \phi(1680)\gamma)}{\mathcal{B}(B_s^0 \rightarrow \phi(1020)\gamma)} \times \mathcal{B}(\phi(1680) \rightarrow K^+K^-) = 0.026^{+0.004}_{-0.003} \text{ (stat.)} \pm 0.005 \text{ (syst.)}.$$

The mass and width of the $f'_2(1525)$ meson are measured, identically for all the almost degenerate solutions, as

$$\begin{aligned} \mu_{f'_2(1525)} &= 1521.8 \pm 1.7 \text{ (stat.)} \text{ }^{+1.4}_{-1.9} \text{ (syst.) MeV}/c^2, \\ \Gamma_{f'_2(1525)} &= 79.3 \pm 3.5 \text{ (stat.)} \text{ }^{+3.3}_{-1.5} \text{ (syst.) MeV}/c^2, \end{aligned}$$

in good agreement with the current world average [11] and with the previous LHCb measurement [48]. The precise measurement of the $\phi(1020)$ parameters gives

$$\begin{aligned} \mu_{\phi(1020)} &= 1019.50 \pm 0.02 \text{ (stat.)} \pm 0.02 \text{ (syst.) MeV}/c^2, \\ \Gamma_{\phi(1020)} &= 4.36 \pm 0.05 \text{ (stat.)} \text{ }^{+0.03}_{-0.10} \text{ (syst.) MeV}/c^2, \end{aligned}$$

consistent with their current world average within 1.5 standard deviations. The corresponding Blatt–Weisskopf radius parameter is measured to be

$$r_\phi = 1.0 \pm 0.2 \text{ (stat.)} \pm 0.1 \text{ (syst.) (GeV}/c)^{-1}.$$

Acknowledgements

We express our gratitude to our colleagues in the CERN accelerator departments for the excellent performance of the LHC. We thank the technical and administrative staff at the LHCb institutes. We acknowledge support from CERN and from the national agencies: CAPES, CNPq, FAPERJ and FINEP (Brazil); MOST and NSFC (China); CNRS/IN2P3 (France); BMBF, DFG and MPG (Germany); INFN (Italy); NWO (Netherlands); MNiSW and NCN (Poland); MCID/IFA (Romania); MICINN (Spain); SNSF and SER (Switzerland); NASU (Ukraine); STFC (United Kingdom); DOE NP and NSF (USA). We acknowledge the computing resources that are provided by CERN, IN2P3 (France), KIT and DESY (Germany), INFN (Italy), SURF (Netherlands), PIC (Spain), GridPP (United Kingdom), CSCS (Switzerland), IFIN-HH (Romania), CBPF (Brazil), and Polish WLCG (Poland). We are indebted to the communities behind the multiple open-source software packages on which we depend. Individual groups or members have received support from ARC and ARDC (Australia); Key Research Program of Frontier Sciences of CAS, CAS PIFI, CAS CCEPP, Fundamental Research Funds for the Central Universities, and Sci. & Tech. Program of Guangzhou (China); Minciencias (Colombia); EPLANET, Marie Skłodowska-Curie Actions, ERC and NextGenerationEU (European Union); A*MIDEX, ANR, IPhU and Labex P2IO, and Région Auvergne-Rhône-Alpes (France); AvH Foundation (Germany); ICSC (Italy); GVA, XuntaGal, GENCAT, Inditex, InTalent and Prog. Atracción Talento, CM (Spain); SRC (Sweden); the Leverhulme Trust, the Royal Society and UKRI (United Kingdom).

Appendices

A Fit minima pattern

Table 4 reports the fit fractions and the integrated interference fractions, $\mathcal{I}(R_1, R_2) = \int [|\mathcal{A}_{R_1} + \mathcal{A}_{R_2}|^2 - |\mathcal{A}_{R_1}|^2 - |\mathcal{A}_{R_2}|^2]$, for the quasi-degenerated fit minima. The corresponding isobar coefficients and relative phases are given in Table 5. The quoted symmetrical errors correspond to the asymptotically correct estimation of the statistical intervals.

Table 4: Fit fractions, \mathcal{F}_R , and interference fractions, $\mathcal{I}(R_1, R_2)$, in the mass range $m_{KK} \in [2m_K, 2400]$ MeV/ c^2 , for (top) the even-spin components and (bottom) the odd-spin components for the fit minima (left) X_i and (right) Y_i . The total integrated interference, $\mathcal{I}_{\{R_P\}}$, and the overall fit fraction, $\mathcal{F}_{\{R_P\}}$ for the odd- ($R_- = \phi$) and the even-spin ($R_+ = f_2$) subsystems are emphasised.

$\Delta \ln \mathcal{L}$	0.0 (X_0)	0.1 (X_1)	0.5 (X_2)	0.6 (X_3)	1.5 (Y_0)	1.6 (Y_1)	2.5 (Y_2)	2.9 (Y_3)
$\mathbf{J^{PC} = 2^{++}}$	$\mathcal{F}_{\{f_2\}} = \mathbf{16.8 \pm 0.5 \%$				$\mathcal{F}_{\{f_2\}} = \mathbf{17.3 \pm 0.6 \%$			
$\mathcal{F}_{f_2(1525)}$	12.1 \pm 0.5	13.8 \pm 0.6	17.9 \pm 0.7	20.4 \pm 0.8	12.2 \pm 0.5	13.9 \pm 0.6	18.3 \pm 0.8	20.8 \pm 0.8
$\mathcal{F}_{f_2(1270)}$	0.8 \pm 0.3	0.9 \pm 0.3	2.9 \pm 0.5	3.2 \pm 0.6	0.9 \pm 0.3	0.9 \pm 0.3	3.1 \pm 0.5	3.4 \pm 0.6
$\mathcal{F}_{f_2(2010)}$	0.4 \pm 0.2	3.7 \pm 0.5	0.5 \pm 0.2	4.1 \pm 0.8	0.5 \pm 0.2	4.3 \pm 0.6	0.6 \pm 0.2	4.8 \pm 0.6
$\mathcal{I}(f_2'(1525), f_2(1270))$	+2.4 \pm 0.4	+2.3 \pm 0.6	-5.7 \pm 0.7	-6.3 \pm 0.6	+2.6 \pm 0.4	+2.7 \pm 0.5	-6.1 \pm 0.7	-6.5 \pm 0.6
$\mathcal{I}(f_2'(1525), f_2(2010))$	+0.7 \pm 0.4	-3.1 \pm 0.6	+1.7 \pm 0.4	-4.9 \pm 0.4	+0.8 \pm 0.4	-3.5 \pm 0.6	+1.9 \pm 0.3	-5.3 \pm 0.4
$\mathcal{I}(f_2(2010), f_2(1270))$	+0.3 \pm 0.1	-0.7 \pm 0.4	-0.5 \pm 0.3	+0.3 \pm 0.5	+0.4 \pm 0.1	-1.0 \pm 0.3	-0.5 \pm 0.3	+0.1 \pm 0.4
$\mathcal{I}_{\{f_2\}}$	+3.5 \pm 0.5	-1.5 \pm 0.5	-4.6 \pm 0.9	-11.0 \pm 1.1	+3.8 \pm 0.5	-1.8 \pm 0.5	-4.7 \pm 0.8	-11.8 \pm 1.0
$\mathbf{J^{PC} = (1, 3)^{--}}$	$\mathcal{F}_{\{\phi\}} = \mathbf{83.2 \pm 0.5 \%$				$\mathcal{F}_{\{\phi\}} = \mathbf{82.7 \pm 0.6 \%$			
$\mathcal{F}_{\phi(1020)}$	70.4 \pm 1.0				71.1 \pm 0.7			
$\mathcal{F}_{\phi(1680)}$	4.0 \pm 0.5				18.2 \pm 1.0			
$\mathcal{F}_{\phi_3(1850)}$	0.3 \pm 0.1				0.2 \pm 0.1			
$\mathcal{F}_{(KK)_{NR}}$	0.4 \pm 0.3				0.3 \pm 0.2			
$\mathcal{I}(\phi_3(1850), \phi(1680))$	+3.9 \pm 0.3				-7.8 \pm 0.5			
$\mathcal{I}(\phi(1020), (KK)_{NR})$	+4.0 \pm 1.2				+2.7 \pm 1.0			
$\mathcal{I}(\phi(1680), (KK)_{NR})$	+0.3 \pm 0.2				-2.0 \pm 0.8			
$\mathcal{I}(\phi_3(1850), \phi_1)$	0				0			
$\mathcal{I}_{\{\phi\}}$	+8.1 \pm 1.0				-7.2 \pm 0.6			

Table 5: Isobar coefficients and phases for (top) the fit minima X_i and (bottom) Y_i .

	X_0		X_1		X_2		X_3	
	$ c_R $ [$\times 10$]	δ_R [deg.]	$ c_R $ [$\times 10$]	δ_R [deg.]	$ c_R $ [$\times 10$]	δ_R [deg.]	$ c_R $ [$\times 10$]	δ_R [deg.]
$\phi(1020)$	10	0	10	0	10	0	10	0
$\phi(1680)$	2.40 \pm 0.15	138 \pm 4	2.39 \pm 0.14	138 \pm 4	2.38 \pm 0.14	138 \pm 4	2.38 \pm 0.14	137 \pm 4
$\phi_3(1850)$	0.61 \pm 0.16	-61 \pm 13	0.61 \pm 0.15	-61 \pm 12	0.60 \pm 0.16	-61 \pm 13	0.60 \pm 0.16	-61 \pm 13
$(KK)_{NR}$	0.79 \pm 0.26	165 \pm 8	0.80 \pm 0.21	165 \pm 6	0.81 \pm 0.21	165 \pm 6	0.81 \pm 0.21	164 \pm 7
$f_2'(1525)$	4.16 \pm 0.09	0	4.43 \pm 0.10	0	5.04 \pm 0.12	0	5.38 \pm 0.11	0
$f_2(1270)$	1.07 \pm 0.17	-55 \pm 14	1.11 \pm 0.17	-72 \pm 16	2.04 \pm 0.19	146 \pm 7	2.13 \pm 0.19	130 \pm 6
$f_2(2010)$	0.74 \pm 0.18	42 \pm 26	2.29 \pm 0.17	-122 \pm 10	0.86 \pm 0.20	93 \pm 28	2.43 \pm 0.18	68 \pm 8
	Y_0		Y_1		Y_2		Y_3	
$\phi(1020)$	10	0	10	0	10	0	10	0
$\phi(1680)$	5.06 \pm 0.15	-135 \pm 3	5.07 \pm 0.15	-135 \pm 3	5.09 \pm 0.15	-134 \pm 3	5.09 \pm 0.15	-134 \pm 3
$\phi_3(1850)$	0.57 \pm 0.17	116 \pm 23	0.56 \pm 0.17	116 \pm 24	0.55 \pm 0.18	117 \pm 25	0.53 \pm 0.18	117 \pm 26
$(KK)_{NR}$	0.59 \pm 0.22	137 \pm 14	0.59 \pm 0.22	137 \pm 14	0.60 \pm 0.22	137 \pm 14	0.60 \pm 0.23	136 \pm 15
$f_2'(1525)$	4.13 \pm 0.09	0	4.41 \pm 0.10	0	5.06 \pm 0.11	0	5.41 \pm 0.11	0
$f_2(1270)$	1.09 \pm 0.17	-43 \pm 13	1.14 \pm 0.18	-60 \pm 14	2.08 \pm 0.18	142 \pm 7	2.18 \pm 0.19	125 \pm 5
$f_2(2010)$	0.81 \pm 0.15	44 \pm 22	2.47 \pm 0.17	-121 \pm 9	0.92 \pm 0.17	92 \pm 24	2.59 \pm 0.17	-68 \pm 7

References

- [1] CLEO collaboration, R. Ammar *et al.*, *Evidence for penguins: First observation of $B \rightarrow K^*(892)\gamma$* , Phys. Rev. Lett. **71** (1993) 674.
- [2] Belle collaboration, D. Dutta *et al.*, *Search for $B_s^0 \rightarrow \gamma\gamma$ and a measurement of the branching fraction for $B_s^0 \rightarrow \phi\gamma$* , Phys. Rev. **D91** (2015) 011101, arXiv:1411.7771.
- [3] LHCb collaboration, R. Aaij *et al.*, *Measurement of the ratio of branching fractions $\mathcal{B}(B^0 \rightarrow K^{*0}\gamma)/\mathcal{B}(B_s^0 \rightarrow \phi\gamma)$ and the direct CP asymmetry in $B^0 \rightarrow K^{*0}\gamma$* , Nucl. Phys. **B867** (2013) 1, arXiv:1209.0313.
- [4] LHCb collaboration, R. Aaij *et al.*, *First experimental study of photon polarization in radiative B_s^0 decays*, Phys. Rev. Lett. **118** (2017) 021801, arXiv:1609.02032.
- [5] LHCb collaboration, R. Aaij *et al.*, *Measurement of CP-violating and mixing-induced observables in $B_s^0 \rightarrow \phi\gamma$ decays*, Phys. Rev. Lett. **123** (2019) 081802, arXiv:1905.06284.
- [6] LHCb collaboration, R. Aaij *et al.*, *Observation of photon polarization in the $b \rightarrow s\gamma$ transition*, Phys. Rev. Lett. **112** (2014) 161801, arXiv:1402.6852.
- [7] LHCb collaboration, R. Aaij *et al.*, *First observation of the radiative $\Lambda_b^0 \rightarrow \Lambda\gamma$ decay*, Phys. Rev. Lett. **123** (2019) 031801, arXiv:1904.06697.
- [8] LHCb collaboration, R. Aaij *et al.*, *Measurement of the photon polarization in $\Lambda_b^0 \rightarrow \Lambda\gamma$ decays*, Phys. Rev. **D105** (2022) 051104, arXiv:2111.10194.
- [9] LHCb collaboration, R. Aaij *et al.*, *Search for the radiative $\Xi_b^- \rightarrow \Xi^-\gamma$ decay*, JHEP **01** (2022) 069, arXiv:2108.07678.
- [10] LHCb collaboration, R. Aaij *et al.*, *Amplitude analysis of the $\Lambda_b^0 \rightarrow pK^-\gamma$ decay*, arXiv:2403.03710.
- [11] Particle Data Group, R. L. Workman *et al.*, *Review of particle physics*, Prog. Theor. Exp. Phys. **2022** (2022) 083C01.
- [12] A. Ali, T. Ohl, and T. Mannel, *Radiative rare B decays into higher K-resonances*, Phys. Lett. **B298** (1993) 195–203.
- [13] D. Atwood, M. Gronau, and A. Soni, *Mixing-induced CP asymmetries in radiative B decays in and beyond the standard model*, Phys. Rev. Lett. **79** (1997) 185–188.
- [14] S. Veseli and M. G. Olsson, *Radiative rare B decays revisited*, Phys. Lett. **B367** (1996) 309.
- [15] D. Ebert, R. N. Faustov, V. O. Galkin, and H. Toki, *Rare radiative B decays to orbitally excited K mesons*, Phys. Rev. **D64** (2001) 054001, arXiv:hep-ph/0104264.
- [16] BaBar collaboration, J. P. Lees *et al.*, *Dalitz plot analyses of $J/\psi \rightarrow \pi^+\pi^-\pi^0$, $J/\psi \rightarrow K^+K^-\pi^0$, and $J/\psi \rightarrow K_s^0K^\pm\pi^\mp$ produced via e^+e^- annihilation with initial-state radiation*, Phys. Rev. **D95** (2017) 072007.

- [17] LHCb collaboration, A. A. Alves Jr. *et al.*, *The LHCb detector at the LHC*, JINST **3** (2008) S08005.
- [18] LHCb collaboration, R. Aaij *et al.*, *LHCb detector performance*, Int. J. Mod. Phys. **A30** (2015) 1530022, [arXiv:1412.6352](#).
- [19] T. Sjöstrand, S. Mrenna, and P. Skands, *A brief introduction to PYTHIA 8.1*, Comput. Phys. Commun. **178** (2008) 852, [arXiv:0710.3820](#).
- [20] I. Belyaev *et al.*, *Handling of the generation of primary events in Gauss, the LHCb simulation framework*, Nuclear Science Symposium Conference Record (NSS/MIC) **IEEE** (2010) 1155.
- [21] D. J. Lange, *The EvtGen particle decay simulation package*, Nucl. Instrum. Meth. **A462** (2001) 152.
- [22] P. Golonka and Z. Was, *PHOTOS Monte Carlo: A precision tool for QED corrections in Z and W decays*, Eur. Phys. J. **C45** (2006) 97, [arXiv:hep-ph/0506026](#).
- [23] Geant4 collaboration, S. Agostinelli *et al.*, *Geant4: A simulation toolkit*, Nucl. Instrum. Meth. **A506** (2003) 250.
- [24] Geant4 collaboration, J. Allison *et al.*, *Geant4 developments and applications*, IEEE Trans. Nucl. Sci. **53** (2006) 270.
- [25] R. Aaij *et al.*, *The LHCb trigger and its performance in 2011*, JINST **8** (2013) P04022, [arXiv:1211.3055](#).
- [26] LHCb collaboration, R. Aaij *et al.*, *Design and performance of the LHCb trigger and full real-time reconstruction in Run 2 of the LHC*, JINST **14** (2018) P04013. 43 p.
- [27] A. Puig, *The HLT2 radiative topological lines*, LHCb-PUB-2012-002. CERN-LHCb-PUB-2012-002, CERN, Geneva, 2012.
- [28] T. Likhomanenko *et al.*, *LHCb topological trigger reoptimization*, J. Phys. Conf. Ser. **664** (2015) 082025, [arXiv:1510.00572](#).
- [29] L. Anderlini *et al.*, *The PIDCalib package*, LHCb-PUB-2016-021, 2016.
- [30] M. Calvo Gomez *et al.*, *A tool for γ/π^0 separation at high energies*, LHCb-PUB-2015-016. CERN-LHCb-PUB-2015-016, CERN, Geneva, 2015.
- [31] L. Breiman, J. H. Friedman, R. A. Olshen, and C. J. Stone, *Classification and regression trees*, Statistics/Probability Series, Wadsworth Publishing Company, Belmont, California, U.S.A., 1984.
- [32] B. P. Roe *et al.*, *Boosted decision trees, an alternative to artificial neural networks*, Nucl. Instrum. Meth. **A543** (2005) 577, [arXiv:physics/0408124](#).
- [33] J. E. Gaiser, *Charmonium spectroscopy from radiative decays of the J/ψ and ψ'* , PhD thesis, SLAC-R-255 (1982).

- [34] ARGUS collaboration, H. Albrecht *et al.*, *Search for hadronic $b \rightarrow u$ decays*, Phys. Lett. **B241** (1990) 278.
- [35] M. Pivk and F. R. Le Diberder, *sPlot: a statistical tool to unfold data distributions*, Nucl. Instrum. Meth. **A555** (2005) 356, [arXiv:physics/0402083](#).
- [36] R. H. Dalitz, *On the analysis of tau-meson data and the nature of the tau-meson*, Phil. Mag. Ser. 7 **44** (1953) 1068.
- [37] E. P. Wigner, *Group theory and its application to the quantum mechanics of atomic spectra*, Academic Press Inc. , New York (1960) .
- [38] J. M. Blatt and V. F. Weisskopf, *Theoretical nuclear physics*, John Wiley and Sons, New York, 1952.
- [39] R. A. Kycia and S. Jadach, *Relativistic Voigt profile for unstable particles in high energy physics*, J. Math. Anal. Appl. **463** (2018) 1040, [arXiv:1711.09304](#).
- [40] LHCb collaboration, R. Aaij *et al.*, *Measurement of the \bar{B}^0-B^0 and $\bar{B}_s^0-B_s^0$ production asymmetries in pp collisions at $\sqrt{s}=7\text{ TeV}$* , Phys. Lett. **B739** (2014) 218, [arXiv:1408.0275](#).
- [41] M. Matsumori, A. I. Sanda, and Y.-Y. Keum, *CP asymmetry, branching ratios, and isospin breaking effects of $B \rightarrow K^*\gamma$ with the perturbative QCD approach*, Phys. Rev. **D72** (2005) .
- [42] Belle collaboration, C. P. Shen *et al.*, *Observation of the $\phi(1680)$ and the $Y(2175)$ in $e^+e^- \rightarrow \phi\pi^+\pi^-$* , Phys. Rev. **D80** (2009) 031101.
- [43] C. Langenbruch, *Parameter uncertainties in weighted unbinned maximum likelihood fits*, Eur. Phys. J. **C82** (2022) 393.
- [44] H. Dembinski, M. Kenzie, C. Langenbruch, and M. Schmelling, *Custom Orthogonal Weight functions (COWs) for event classification*, Nucl. Instrum. Meth. **A1040** (2022) 167270, [arXiv:2112.04574](#).
- [45] BaBar collaboration, J. P. Lees *et al.*, *Cross sections for the reactions $e^+e^- \rightarrow K^+K^-\pi^+\pi^-$, $K^+K^-\pi^0\pi^0$, and $K^+K^-K^+K^-$ measured using initial-state radiation events*, Phys. Rev. **D86** (2012) 012008.
- [46] D. Bisello *et al.*, *Observation of an isoscalar vector meson at approximately $\simeq 1650\text{ MeV}/c^2$ in the $e^+e^- \rightarrow K\bar{K}\pi$ reaction*, Z. Phys. **C52** (1991) 227.
- [47] BaBar collaboration, B. Aubert *et al.*, *Measurements of $e^+e^- \rightarrow K^+K^-\eta$, $K^+K^-\pi^0$, and $K_s^0K^\pm\pi^\mp$ cross sections using initial state radiation events*, Phys. Rev. **D77** (2008) 092002.
- [48] LHCb collaboration, R. Aaij *et al.*, *Resonances and CP-violation in B_s^0 and $\bar{B}_s^0 \rightarrow J/\psi K^+K^-$ decays in the mass region above the $\phi(1020)$* , JHEP **08** (2017) 037, [arXiv:1704.08217](#).

- [49] A. Rogozhnikov, *Reweighting with boosted decision trees*, Journal of Physics: Conference Series **762** (2016) 012036.
- [50] Belle collaboration, J. H. Kim *et al.*, *Search for $B \rightarrow \phi\pi$ decays*, Phys. Rev. **D86** (2012) 031101, [arXiv:1206.4760](#).
- [51] Belle collaboration, V. Gaur *et al.*, *Evidence for the decay $B^0 \rightarrow K^+K^-\pi^0$* , Phys. Rev. **D87** (2013) 091101, [arXiv:1304.5312](#).
- [52] BaBar collaboration, B. Aubert *et al.*, *Observation of the decay $B^+ \rightarrow K^+K^-\pi^+$* , Phys. Rev. Lett. **99** (2007) 221801.
- [53] LHCb collaboration, R. Aaij *et al.*, *Amplitude analysis of $B^\pm \rightarrow \pi^\pm K^+K^-$ decays*, Phys. Rev. Lett. **123** (2019) 231802, [arXiv:1905.09244](#).
- [54] M. Ablikim *et al.*, *Resonances in $J/\psi \rightarrow \phi\pi^+\pi^-$ and ϕK^+K^-* , Phys. Lett. **B607** (2005) 243.
- [55] F. von Hippel and C. Quigg, *Centrifugal-barrier effects in resonance partial decay widths, shapes, and production amplitudes*, Phys. Rev. **D5** (1972) 624.

LHCb collaboration

R. Aaij³⁶ , A.S.W. Abdelmotteleb⁵⁵ , C. Abellan Beteta⁴⁹ , F. Abudinén⁵⁵ ,
 T. Ackernley⁵⁹ , A. A. Adefisoye⁶⁷ , B. Adeva⁴⁵ , M. Adinolfi⁵³ , P. Adlarson⁷⁹ ,
 C. Agapopoulou⁴⁷ , C.A. Aidala⁸⁰ , Z. Ajaltouni¹¹ , S. Akar⁶⁴ , K. Akiba³⁶ ,
 P. Albicocco²⁶ , J. Albrecht¹⁸ , F. Alessio⁴⁷ , M. Alexander⁵⁸ , Z. Aliouche⁶¹ ,
 P. Alvarez Cartelle⁵⁴ , R. Amalric¹⁵ , S. Amato³ , J.L. Amey⁵³ , Y. Amhis^{13,47} ,
 L. An⁶ , L. Anderlini²⁵ , M. Andersson⁴⁹ , A. Andreianov⁴² , P. Andreola⁴⁹ ,
 M. Andreotti²⁴ , D. Andreou⁶⁷ , A. Anelli^{29,p} , D. Ao⁷ , F. Archilli^{35,v} ,
 M. Argenton²⁴ , S. Arguedas Cuendis⁹ , A. Artamonov⁴² , M. Artuso⁶⁷ ,
 E. Aslanides¹² , M. Atzeni⁶³ , B. Audurier¹⁴ , D. Bacher⁶² , I. Bachiller Perea¹⁰ ,
 S. Bachmann²⁰ , M. Bachmayer⁴⁸ , J.J. Back⁵⁵ , P. Baladron Rodriguez⁴⁵ ,
 V. Balagura¹⁴ , W. Baldini²⁴ , H. Bao⁷ , J. Baptista de Souza Leite⁵⁹ ,
 M. Barbetti^{25,m} , I. R. Barbosa⁶⁸ , R.J. Barlow⁶¹ , M. Barnyakov²³ , S. Barsuk¹³ ,
 W. Barter⁵⁷ , M. Bartolini⁵⁴ , J. Bartz⁶⁷ , F. Baryshnikov⁴² , J.M. Basels¹⁶ ,
 G. Bassi³³ , B. Batsukh⁵ , A. Battig¹⁸ , A. Bay⁴⁸ , A. Beck⁵⁵ , M. Becker¹⁸ ,
 F. Bedeschi³³ , I.B. Bediaga² , S. Belin⁴⁵ , V. Bellee⁴⁹ , K. Belous⁴² , I. Belov²⁷ ,
 I. Belyaev³⁴ , G. Benane¹² , G. Bencivenni²⁶ , E. Ben-Haim¹⁵ , A. Berezhnoy⁴² ,
 R. Bernet⁴⁹ , S. Bernet Andres⁴³ , A. Bertolin³¹ , C. Betancourt⁴⁹ , F. Betti⁵⁷ , J.
 Bex⁵⁴ , I.a. Bezshyiko⁴⁹ , J. Bhom³⁹ , M.S. Bieker¹⁸ , N.V. Biesuz²⁴ , P. Billoir¹⁵ ,
 A. Biolchini³⁶ , M. Birch⁶⁰ , F.C.R. Bishop¹⁰ , A. Bitadze⁶¹ , A. Bizzeti , T. Blake⁵⁵ ,
 F. Blanc⁴⁸ , J.E. Blank¹⁸ , S. Blusk⁶⁷ , V. Bocharnikov⁴² , J.A. Boelhave¹⁸ ,
 O. Boente Garcia¹⁴ , T. Boettcher⁶⁴ , A. Bohare⁵⁷ , A. Boldyrev⁴² , C.S. Bolognani⁷⁶ ,
 R. Bolzonella^{24,l} , N. Bondar⁴² , F. Borgato^{31,q,47} , S. Borghi⁶¹ , M. Borsato^{29,p} ,
 J.T. Borsuk³⁹ , S.A. Bouchiba⁴⁸ , T.J.V. Bowcock⁵⁹ , A. Boyer⁴⁷ , C. Bozzi²⁴ ,
 M.J. Bradley⁶⁰ , A. Brea Rodriguez⁴⁵ , N. Breer¹⁸ , J. Brodzicka³⁹ ,
 A. Brossa Gonzalo⁴⁵ , J. Brown⁵⁹ , D. Brundu³⁰ , E. Buchanan⁵⁷ , A. Buonauro⁴⁹ ,
 L. Buonincontri^{31,q} , A.T. Burke⁶¹ , C. Burr⁴⁷ , A. Butkevich⁴² , J.S. Butter⁵⁴ ,
 J. Buytaert⁴⁷ , W. Byczynski⁴⁷ , S. Cadeddu³⁰ , H. Cai⁷² , R. Calabrese^{24,l} ,
 S. Calderon Ramirez⁹ , L. Calefice⁴⁴ , S. Cali²⁶ , M. Calvi^{29,p} , M. Calvo Gomez⁴³ ,
 P. Camargo Magalhaes^{2,z} , J. I. Cambon Bouzas⁴⁵ , P. Campana²⁶ ,
 D.H. Campora Perez⁷⁶ , A.F. Campoverde Quezada⁷ , S. Capelli²⁹ , L. Capriotti²⁴ ,
 R. Caravaca-Mora⁹ , A. Carbone^{23,j} , L. Carcedo Salgado⁴⁵ , R. Cardinale^{27,n} ,
 A. Cardini³⁰ , P. Carniti^{29,p} , L. Carus²⁰ , A. Casais Vidal⁶³ , R. Caspary²⁰ ,
 G. Casse⁵⁹ , J. Castro Godinez⁹ , M. Cattaneo⁴⁷ , G. Cavallero^{24,47} , V. Cavallini^{24,l} ,
 S. Celani²⁰ , D. Cervenkov⁶² , S. Cesare^{28,o} , A.J. Chadwick⁵⁹ , I. Chahrour⁸⁰ ,
 M. Charles¹⁵ , Ph. Charpentier⁴⁷ , C.A. Chavez Barajas⁵⁹ , M. Chefdeville¹⁰ ,
 C. Chen¹² , S. Chen⁵ , Z. Chen⁷ , A. Chernov³⁹ , S. Chernyshenko⁵¹ ,
 V. Chobanova⁷⁸ , S. Cholak⁴⁸ , M. Chrzaszcz³⁹ , A. Chubykin⁴² , V. Chulikov⁴² ,
 P. Ciambrone²⁶ , X. Cid Vidal⁴⁵ , G. Ciezarek⁴⁷ , P. Cifra⁴⁷ , P.E.L. Clarke⁵⁷ ,
 M. Clemencic⁴⁷ , H.V. Cliff⁵⁴ , J. Closier⁴⁷ , C. Cocha Toapaxi²⁰ , V. Coco⁴⁷ ,
 J. Cogan¹² , E. Cogneras¹¹ , L. Cojocariu⁴¹ , P. Collins⁴⁷ , T. Colombo⁴⁷ ,
 A. Comerma-Montells⁴⁴ , L. Congedo²² , A. Contu³⁰ , N. Cooke⁵⁸ , I. Corredoira⁴⁵ ,
 A. Correia¹⁵ , G. Corti⁴⁷ , J.J. Cottee Meldrum⁵³ , B. Couturier⁴⁷ , D.C. Craik⁴⁹ ,
 M. Cruz Torres^{2,g} , E. Curras Rivera⁴⁸ , R. Currie⁵⁷ , C.L. Da Silva⁶⁶ , S. Dadabaev⁴² ,
 L. Dai⁶⁹ , X. Dai⁶ , E. Dall'Occo¹⁸ , J. Dalseno⁴⁵ , C. D'Ambrosio⁴⁷ , J. Daniel¹¹ ,
 A. Danilina⁴² , P. d'Argent²² , A. Davidson⁵⁵ , J.E. Davies⁶¹ , A. Davis⁶¹ ,
 O. De Aguiar Francisco⁶¹ , C. De Angelis^{30,k} , F. De Benedetti⁴⁷ , J. de Boer³⁶ ,
 K. De Bruyn⁷⁵ , S. De Capua⁶¹ , M. De Cian^{20,47} , U. De Freitas Carneiro Da Graca^{2,b} ,
 E. De Lucia²⁶ , J.M. De Miranda² , L. De Paula³ , M. De Serio^{22,h} , P. De Simone²⁶ ,

F. De Vellis¹⁸ , J.A. de Vries⁷⁶ , F. Debernardis²² , D. Decamp¹⁰ , V. Dedu¹² ,
 L. Del Buono¹⁵ , B. Delaney⁶³ , H.-P. Dembinski¹⁸ , J. Deng⁸ , V. Denysenko⁴⁹ ,
 O. Deschamps¹¹ , F. Dettori^{30,k} , B. Dey⁷⁴ , P. Di Nezza²⁶ , I. Diachkov⁴² ,
 S. Didenko⁴² , S. Ding⁶⁷ , L. Dittmann²⁰ , V. Dobishuk⁵¹ , A. D. Docheva⁵⁸ ,
 C. Dong⁴ , A.M. Donohoe²¹ , F. Dordei³⁰ , A.C. dos Reis² , A. D. Dowling⁶⁷ ,
 W. Duan⁷⁰ , P. Duda⁷⁷ , M.W. Dudek³⁹ , L. Dufour⁴⁷ , V. Duk³² , P. Durante⁴⁷ , M.
 M. Duras⁷⁷ , J.M. Durham⁶⁶ , O. D. Durmus⁷⁴ , A. Dziurda³⁹ , A. Dzyuba⁴² ,
 S. Easo⁵⁶ , E. Eckstein¹⁷ , U. Egede¹ , A. Egorychev⁴² , V. Egorychev⁴² ,
 S. Eisenhardt⁵⁷ , E. Ejopu⁶¹ , S. Ek-In⁴⁸ , L. Eklund⁷⁹ , M. Elashri⁶⁴ ,
 J. Ellbracht¹⁸ , S. Ely⁶⁰ , A. Ene⁴¹ , E. Epple⁶⁴ , J. Eschle⁶⁷ , S. Esen²⁰ ,
 T. Evans⁶¹ , F. Fabiano^{30,k,47} , L.N. Falcao² , Y. Fan⁷ , B. Fang⁷² , L. Fantini^{32,r} ,
 M. Faria⁴⁸ , K. Farmer⁵⁷ , D. Fazzini^{29,p} , L. Felkowski⁷⁷ , M. Feng^{5,7} , M. Feo^{18,47} ,
 M. Fernandez Gomez⁴⁵ , A.D. Fernez⁶⁵ , F. Ferrari²³ , F. Ferreira Rodrigues³ ,
 S. Ferreres Sole³⁶ , M. Ferrillo⁴⁹ , M. Ferro-Luzzi⁴⁷ , S. Filippov⁴² , R.A. Fini²² ,
 M. Fiorini^{24,l} , K.M. Fischer⁶² , D.S. Fitzgerald⁸⁰ , C. Fitzpatrick⁶¹ , F. Fleuret¹⁴ ,
 M. Fontana²³ , L. F. Foreman⁶¹ , R. Forty⁴⁷ , D. Foulds-Holt⁵⁴ , M. Franco Sevilla⁶⁵ ,
 M. Frank⁴⁷ , E. Franzoso^{24,l} , G. Frau²⁰ , C. Frei⁴⁷ , D.A. Friday⁶¹ , J. Fu⁷ ,
 Q. Fuehring¹⁸ , Y. Fujii¹ , T. Fulghesu¹⁵ , E. Gabriel³⁶ , G. Galati²² , M.D. Galati³⁶ ,
 A. Gallas Torreira⁴⁵ , D. Galli^{23,j} , S. Gambetta⁵⁷ , M. Gandelman³ , P. Gandini²⁸ , B.
 Ganie⁶¹ , H. Gao⁷ , R. Gao⁶² , Y. Gao⁸ , Y. Gao⁶ , Y. Gao⁸ , M. Garau^{30,k} ,
 L.M. Garcia Martin⁴⁸ , P. Garcia Moreno⁴⁴ , J. García Pardiñas⁴⁷ , K. G. Garg⁸ ,
 L. Garrido⁴⁴ , C. Gaspar⁴⁷ , R.E. Geertsema³⁶ , L.L. Gerken¹⁸ , E. Gersabeck⁶¹ ,
 M. Gersabeck⁶¹ , T. Gershon⁵⁵ , Z. Ghorbanimoghaddam⁵³ , L. Giambastiani^{31,q} , F.
 I. Giasemis^{15,e} , V. Gibson⁵⁴ , H.K. Giemza⁴⁰ , A.L. Gilman⁶² , M. Giovannetti²⁶ ,
 A. Gioventù⁴⁴ , P. Gironella Gironell⁴⁴ , C. Giugliano^{24,l} , M.A. Giza³⁹ ,
 E.L. Gkoukousis⁶⁰ , F.C. Glaser^{13,20} , V.V. Gligorov¹⁵ , C. Göbel⁶⁸ , E. Golobardes⁴³ ,
 D. Golubkov⁴² , A. Golutvin^{60,42,47} , A. Gomes^{2,a,†} , S. Gomez Fernandez⁴⁴ ,
 F. Goncalves Abrantes⁶² , M. Goncerz³⁹ , G. Gong⁴ , J. A. Gooding¹⁸ , I.V. Gorelov⁴² ,
 C. Gotti²⁹ , J.P. Grabowski¹⁷ , L.A. Granado Cardoso⁴⁷ , E. Graugés⁴⁴ ,
 E. Graverini^{48,t} , L. Grazette⁵⁵ , G. Graziani , A. T. Grecu⁴¹ , L.M. Greeven³⁶ ,
 N.A. Grieser⁶⁴ , L. Grillo⁵⁸ , S. Gromov⁴² , C. Gu¹⁴ , M. Guarise²⁴ , M. Guittiere¹³ ,
 V. Guliaeva⁴² , P. A. Günther²⁰ , A.-K. Guseinov⁴⁸ , E. Gushchin⁴² , Y. Guz^{6,42,47} ,
 T. Gys⁴⁷ , K. Habermann¹⁷ , T. Hadavizadeh¹ , C. Hadjivasiliou⁶⁵ , G. Haefeli⁴⁸ ,
 C. Haen⁴⁷ , J. Haimberger⁴⁷ , M. Hajheidari⁴⁷ , M.M. Halvorsen⁴⁷ , P.M. Hamilton⁶⁵ ,
 J. Hammerich⁵⁹ , Q. Han⁸ , X. Han²⁰ , S. Hansmann-Menzemer²⁰ , L. Hao⁷ ,
 N. Harnew⁶² , M. Hartmann¹³ , J. He^{7,c} , F. Hemmer⁴⁷ , C. Henderson⁶⁴ ,
 R.D.L. Henderson^{1,55} , A.M. Hennequin⁴⁷ , K. Hennessy⁵⁹ , L. Henry⁴⁸ , J. Herd⁶⁰ ,
 P. Herrero Gascon²⁰ , J. Heuel¹⁶ , A. Hicheur³ , G. Hijano Mendizabal⁴⁹ , D. Hill⁴⁸ ,
 S.E. Hollitt¹⁸ , J. Horswill⁶¹ , R. Hou⁸ , Y. Hou¹¹ , N. Howarth⁵⁹ , J. Hu²⁰ , J. Hu⁷⁰ ,
 W. Hu⁶ , X. Hu⁴ , W. Huang⁷ , W. Hulsbergen³⁶ , R.J. Hunter⁵⁵ , M. Hushchyn⁴² ,
 D. Hutchcroft⁵⁹ , D. Ilin⁴² , P. Ilten⁶⁴ , A. Inglessi⁴² , A. Iniukhin⁴² , A. Ishteev⁴² ,
 K. Ivshin⁴² , R. Jacobsson⁴⁷ , H. Jage¹⁶ , S.J. Jaimes Elles^{46,73} , S. Jakobsen⁴⁷ ,
 E. Jans³⁶ , B.K. Jashal⁴⁶ , A. Jawahery^{65,47} , V. Jevtic¹⁸ , E. Jiang⁶⁵ , X. Jiang^{5,7} ,
 Y. Jiang⁷ , Y. J. Jiang⁶ , M. John⁶² , D. Johnson⁵² , C.R. Jones⁵⁴ , T.P. Jones⁵⁵ ,
 S. Joshi⁴⁰ , B. Jost⁴⁷ , N. Jurik⁴⁷ , I. Juszczak³⁹ , D. Kaminaris⁴⁸ , S. Kandybei⁵⁰ ,
 Y. Kang⁴ , C. Kar¹¹ , M. Karacson⁴⁷ , D. Karpenkov⁴² , A. Kauniskangas⁴⁸ ,
 J.W. Kautz⁶⁴ , F. Keizer⁴⁷ , M. Kenzie⁵⁴ , T. Ketel³⁶ , B. Khanji⁶⁷ , A. Kharisova⁴² ,
 S. Kholodenko^{33,47} , G. Khreich¹³ , T. Kirn¹⁶ , V.S. Kirsebom^{29,p} , O. Kitouni⁶³ ,
 S. Klaver³⁷ , N. Kleijne^{33,s} , K. Klimaszewski⁴⁰ , M.R. Kmiec⁴⁰ , S. Koliiev⁵¹ ,
 L. Kolk¹⁸ , A. Konoplyannikov⁴² , P. Kopciwicz^{38,47} , P. Koppenburg³⁶ ,

M. Korolev⁴² , I. Kostiuk³⁶ , O. Kot⁵¹ , S. Kotriakhova , A. Kozachuk⁴² ,
P. Kravchenko⁴² , L. Kravchuk⁴² , M. Kreps⁵⁵ , P. Krokovny⁴² , W. Krupa⁶⁷ ,
W. Krzemien⁴⁰ , O.K. Kshyvanskyi⁵¹ , J. Kubat²⁰ , S. Kubis⁷⁷ , M. Kucharczyk³⁹ ,
V. Kudryavtsev⁴² , E. Kulikova⁴² , A. Kupsc⁷⁹ , B. K. Kutsenko¹² , D. Lacarrere⁴⁷ ,
A. Lai³⁰ , A. Lampis³⁰ , D. Lancierini⁵⁴ , C. Landesa Gomez⁴⁵ , J.J. Lane¹ ,
R. Lane⁵³ , C. Langenbruch²⁰ , J. Langer¹⁸ , O. Lantwin⁴² , T. Latham⁵⁵ ,
F. Lazzari^{33,t} , C. Lazzeroni⁵² , R. Le Gac¹² , R. Lefèvre¹¹ , A. Leflat⁴² ,
S. Legotin⁴² , M. Lehuraux⁵⁵ , E. Lemos Cid⁴⁷ , O. Leroy¹² , T. Lesiak³⁹ ,
B. Leverington²⁰ , A. Li⁴ , H. Li⁷⁰ , K. Li⁸ , L. Li⁶¹ , P. Li⁴⁷ , P.-R. Li⁷¹ , Q.
Li^{5,7} , S. Li⁸ , T. Li^{5,d} , T. Li⁷⁰ , Y. Li⁸ , Y. Li⁵ , Z. Lian⁴ , X. Liang⁶⁷ ,
S. Libralon⁴⁶ , C. Lin⁷ , T. Lin⁵⁶ , R. Lindner⁴⁷ , V. Lisovskyi⁴⁸ , R. Litvinov³⁰ , F.
L. Liu¹ , G. Liu⁷⁰ , K. Liu⁷¹ , S. Liu^{5,7} , Y. Liu⁵⁷ , Y. Liu⁷¹ , Y. L. Liu⁶⁰ ,
A. Lobo Salvia⁴⁴ , A. Loi³⁰ , J. Lomba Castro⁴⁵ , T. Long⁵⁴ , J.H. Lopes³ ,
A. Lopez Huertas⁴⁴ , S. López Soliño⁴⁵ , C. Lucarelli^{25,m} , D. Lucchesi^{31,q} ,
M. Lucio Martinez⁷⁶ , V. Lukashenko^{36,51} , Y. Luo⁶ , A. Lupato³¹ , E. Luppi^{24,l} ,
K. Lynch²¹ , X.-R. Lyu⁷ , G. M. Ma⁴ , R. Ma⁷ , S. Maccolini¹⁸ , F. Machefert¹³ ,
F. Maciuc⁴¹ , B. Mack⁶⁷ , I. Mackay⁶² , L. M. Mackey⁶⁷ , L.R. Madhan Mohan⁵⁴ , M.
M. Madurai⁵² , A. Maevskiy⁴² , D. Magdalinski³⁶ , D. Maisuzenko⁴² ,
M.W. Majewski³⁸ , J.J. Malczewski³⁹ , S. Malde⁶² , L. Malentacca⁴⁷ , A. Malinin⁴² ,
T. Maltsev⁴² , G. Manca^{30,k} , G. Mancinelli¹² , C. Mancuso^{28,13,o} ,
R. Manera Escalero⁴⁴ , D. Manuzzi²³ , D. Marangotto^{28,o} , J.F. Marchand¹⁰ ,
R. Marchevski⁴⁸ , U. Marconi²³ , S. Mariani⁴⁷ , C. Marin Benito⁴⁴ , J. Marks²⁰ ,
A.M. Marshall⁵³ , G. Martelli^{32,r} , G. Martellotti³⁴ , L. Martinazzoli⁴⁷ ,
M. Martinelli^{29,p} , D. Martinez Santos⁴⁵ , F. Martinez Vidal⁴⁶ , A. Massafferri² ,
R. Matev⁴⁷ , A. Mathad⁴⁷ , V. Matiunin⁴² , C. Matteuzzi⁶⁷ , K.R. Mattioli¹⁴ ,
A. Mauri⁶⁰ , E. Maurice¹⁴ , J. Mauricio⁴⁴ , P. Mayencourt⁴⁸ , M. Mazurek⁴⁰ ,
M. McCann⁶⁰ , L. McConnell²¹ , T.H. McGrath⁶¹ , N.T. McHugh⁵⁸ , A. McNab⁶¹ ,
R. McNulty²¹ , B. Meadows⁶⁴ , G. Meier¹⁸ , D. Melnychuk⁴⁰ , F. M. Meng⁴ ,
M. Merk^{36,76} , A. Merli^{28,o} , L. Meyer Garcia³ , D. Miao^{5,7} , H. Miao⁷ ,
M. Mikhasenko^{17,f} , D.A. Milanese⁷³ , A. Minotti^{29,p} , E. Minucci⁶⁷ , T. Miralles¹¹ ,
B. Mitreska¹⁸ , D.S. Mitzel¹⁸ , A. Modak⁵⁶ , A. Mödden¹⁸ , R.A. Mohammed⁶² ,
R.D. Moise¹⁶ , S. Mokhnenko⁴² , T. Mombächer⁴⁷ , M. Monk^{55,1} , S. Monteil¹¹ ,
A. Morcillo Gomez⁴⁵ , G. Morello²⁶ , M.J. Morello^{33,s} , M.P. Morgenthaler²⁰ ,
A.B. Morris⁴⁷ , A.G. Morris¹² , R. Mountain⁶⁷ , H. Mu⁴ , Z. M. Mu⁶ ,
E. Muhammad⁵⁵ , F. Muheim⁵⁷ , M. Mulder⁷⁵ , K. Müller⁴⁹ , F. Muñoz-Rojas⁹ ,
R. Murta⁶⁰ , P. Naik⁵⁹ , T. Nakada⁴⁸ , R. Nandakumar⁵⁶ , T. Nanut⁴⁷ , I. Nasteva³ ,
M. Needham⁵⁷ , N. Neri^{28,o} , S. Neubert¹⁷ , N. Neufeld⁴⁷ , P. Neustroev⁴² ,
J. Nicolini^{18,13} , D. Nicotra⁷⁶ , E.M. Niel⁴⁸ , N. Nikitin⁴² , P. Nogga¹⁷ , N.S. Nolte⁶³ ,
C. Normand⁵³ , J. Novoa Fernandez⁴⁵ , G. Nowak⁶⁴ , C. Nunez⁸⁰ , H. N. Nur⁵⁸ ,
A. Oblakowska-Mucha³⁸ , V. Obraztsov⁴² , T. Oeser¹⁶ , S. Okamura^{24,l,47} ,
A. Okhotnikov⁴² , O. Okhrimenko⁵¹ , R. Oldeman^{30,k} , F. Oliva⁵⁷ , M. Olocco¹⁸ ,
C.J.G. Onderwater⁷⁶ , R.H. O'Neil⁵⁷ , J.M. Otalora Goicochea³ , P. Owen⁴⁹ ,
A. Oyanguren⁴⁶ , O. Ozcelik⁵⁷ , K.O. Padeken¹⁷ , B. Pagare⁵⁵ , P.R. Pais²⁰ ,
T. Pajero⁴⁷ , A. Palano²² , M. Palutan²⁶ , G. Panshin⁴² , L. Paolucci⁵⁵ ,
A. Papanestis⁵⁶ , M. Pappagallo^{22,h} , L.L. Pappalardo^{24,l} , C. Pappenheimer⁶⁴ ,
C. Parkes⁶¹ , B. Passalacqua²⁴ , G. Passaleva²⁵ , D. Passaro^{33,s} , A. Pastore²² ,
M. Patel⁶⁰ , J. Patoc⁶² , C. Patrignani^{23,j} , A. Paul⁶⁷ , C.J. Pawley⁷⁶ ,
A. Pellegrino³⁶ , J. Peng^{5,7} , M. Pepe Altarelli²⁶ , S. Perazzini²³ , D. Pereima⁴² ,
A. Pereiro Castro⁴⁵ , P. Perret¹¹ , A. Perro⁴⁷ , K. Petridis⁵³ , A. Petrolini^{27,n} , J. P.
Pfaller⁶⁴ , H. Pham⁶⁷ , L. Pica^{33,s} , M. Piccini³² , B. Pietrzyk¹⁰ , G. Pietrzyk¹³ ,

D. Pinci³⁴ , F. Pisani⁴⁷ , M. Pizzichemi^{29,p} , V. Placinta⁴¹ , M. Plo Casarus⁴⁵ ,
 F. Polci^{15,47} , M. Poli Lener²⁶ , A. Poluektov¹² , N. Polukhina⁴² , I. Polyakov⁴⁷ ,
 E. Polycarpo³ , S. Ponce⁴⁷ , D. Popov⁷ , S. Poslavskii⁴² , K. Prasanth⁵⁷ ,
 C. Prouve⁴⁵ , V. Pugatch⁵¹ , G. Punzi^{33,t} , S. Qasim⁴⁹ , W. Qian⁷ , N. Qin⁴ ,
 S. Qu⁴ , R. Quagliani⁴⁷ , B. Quintana¹⁰ , R.I. Rabadan Trejo⁵⁵ , J.H. Rademacker⁵³ ,
 M. Rama³³ , M. Ramírez García⁸⁰ , M. Ramos Pernas⁵⁵ , M.S. Rangel³ ,
 F. Ratnikov⁴² , G. Raven³⁷ , M. Rebollo De Miguel⁴⁶ , F. Redi^{28,i} , J. Reich⁵³ ,
 F. Reiss⁶¹ , Z. Ren⁷ , P.K. Resmi⁶² , R. Ribatti^{33,s} , G. R. Ricart^{14,81} ,
 D. Riccardi^{33,s} , S. Ricciardi⁵⁶ , K. Richardson⁶³ , M. Richardson-Slipper⁵⁷ ,
 K. Rinnert⁵⁹ , P. Robbe¹³ , G. Robertson⁵⁸ , E. Rodrigues⁵⁹ ,
 E. Rodriguez Fernandez⁴⁵ , J.A. Rodriguez Lopez⁷³ , E. Rodriguez Rodriguez⁴⁵ ,
 A. Rogovskiy⁵⁶ , D.L. Rolf⁴⁷ , P. Roloff⁴⁷ , V. Romanovskiy⁴² , M. Romero Lamas⁴⁵ ,
 A. Romero Vidal⁴⁵ , G. Romolini²⁴ , F. Ronchetti⁴⁸ , M. Rotonondo²⁶ , S. R. Roy²⁰ ,
 M.S. Rudolph⁶⁷ , T. Ruf⁴⁷ , M. Ruiz Diaz²⁰ , R.A. Ruiz Fernandez⁴⁵ ,
 J. Ruiz Vidal^{79,aa} , A. Ryzhikov⁴² , J. Ryzka³⁸ , J. J. Saavedra-Arias⁹ ,
 J.J. Saborido Silva⁴⁵ , R. Sadek¹⁴ , N. Sagidova⁴² , D. Sahoo⁷⁴ , N. Sahoo⁵² ,
 B. Saitta^{30,k} , M. Salomoni^{29,p,47} , C. Sanchez Gras³⁶ , I. Sanderswood⁴⁶ ,
 R. Santacesaria³⁴ , C. Santamarina Rios⁴⁵ , M. Santimaria^{26,47} , L. Santoro² ,
 E. Santovetti³⁵ , A. Saputi^{24,47} , D. Saranin⁴² , G. Sarpis⁵⁷ , M. Sarpis⁶¹ ,
 C. Satriano^{34,u} , A. Satta³⁵ , M. Saur⁶ , D. Savrina⁴² , H. Sazak¹⁶ ,
 L.G. Scantlebury Smead⁶² , A. Scarabotto¹⁸ , S. Schael¹⁶ , S. Scherl⁵⁹ , M. Schiller⁵⁸ ,
 H. Schindler⁴⁷ , M. Schmelling¹⁹ , B. Schmidt⁴⁷ , S. Schmitt¹⁶ , H. Schmitz¹⁷,
 O. Schneider⁴⁸ , A. Schopper⁴⁷ , N. Schulte¹⁸ , S. Schulte⁴⁸ , M.H. Schune¹³ ,
 R. Schwemmer⁴⁷ , G. Schwering¹⁶ , B. Sciascia²⁶ , A. Sciuccati⁴⁷ , S. Sellam⁴⁵ ,
 A. Semennikov⁴² , T. Senger⁴⁹ , M. Senghi Soares³⁷ , A. Sergi²⁷ , N. Serra⁴⁹ ,
 L. Sestini³¹ , A. Seuthe¹⁸ , Y. Shang⁶ , D.M. Shangase⁸⁰ , M. Shapkin⁴² , R. S.
 Sharma⁶⁷ , I. Shchemerov⁴² , L. Shchutska⁴⁸ , T. Shears⁵⁹ , L. Shekhtman⁴² ,
 Z. Shen⁶ , S. Sheng^{5,7} , V. Shevchenko⁴² , B. Shi⁷ , Q. Shi⁷ , E.B. Shields^{29,p} ,
 Y. Shimizu¹³ , E. Shmanin⁴² , R. Shorkin⁴² , J.D. Shupperd⁶⁷ , R. Silva Coutinho⁶⁷ ,
 G. Simi^{31,q} , S. Simone^{22,h} , N. Skidmore⁵⁵ , T. Skwarnicki⁶⁷ , M.W. Slater⁵² ,
 J.C. Smallwood⁶² , E. Smith⁶³ , K. Smith⁶⁶ , M. Smith⁶⁰ , A. Snoch³⁶ ,
 L. Soares Lavra⁵⁷ , M.D. Sokoloff⁶⁴ , F.J.P. Soler⁵⁸ , A. Solomin^{42,53} , A. Solovev⁴² ,
 I. Solovyev⁴² , R. Song¹ , Y. Song⁴⁸ , Y. Song⁴ , Y. S. Song⁶ ,
 F.L. Souza De Almeida⁶⁷ , B. Souza De Paula³ , E. Spadaro Norella^{28,o} ,
 E. Spedicato²³ , J.G. Speer¹⁸ , E. Spiridenkov⁴² , P. Spradlin⁵⁸ , V. Srisakaran⁴⁷ ,
 F. Stagni⁴⁷ , M. Stahl⁴⁷ , S. Stahl⁴⁷ , S. Stanislaus⁶² , E.N. Stein⁴⁷ , O. Steinkamp⁴⁹ ,
 O. Stenyakin⁴² , H. Stevens¹⁸ , D. Strekalina⁴² , Y. Su⁷ , F. Suljik⁶² , J. Sun³⁰ ,
 L. Sun⁷² , Y. Sun⁶⁵ , D. S. Sundfeld Lima², W. Sutcliffe⁴⁹, P.N. Swallow⁵² ,
 F. Swystun⁵⁴ , A. Szabelski⁴⁰ , T. Szumlak³⁸ , Y. Tan⁴ , M.D. Tat⁶² , A. Terentev⁴⁹ ,
 F. Terzuoli^{33,w} , F. Teubert⁴⁷ , E. Thomas⁴⁷ , D.J.D. Thompson⁵² , H. Tilquin⁶⁰ ,
 V. Tisserand¹¹ , S. T'Jampens¹⁰ , M. Tobin⁵ , L. Tomassetti^{24,l} , G. Tonani^{28,o,47} ,
 X. Tong⁶ , D. Torres Machado² , L. Toscano¹⁸ , D.Y. Tou⁴ , C. Trippi⁴³ , G. Tuci²⁰ ,
 N. Tuning³⁶ , L.H. Uecker²⁰ , A. Ukleja³⁸ , D.J. Unverzagt²⁰ , E. Ursov⁴² ,
 A. Usachov³⁷ , A. Ustyuzhanin⁴² , U. Uwer²⁰ , V. Vagnoni²³ , A. Valassi⁴⁷ ,
 G. Valenti²³ , N. Valls Canudas⁴⁷ , H. Van Hecke⁶⁶ , E. van Herwijnen⁶⁰ ,
 C.B. Van Hulse^{45,y} , R. Van Laak⁴⁸ , M. van Veghel³⁶ , G. Vasquez⁴⁹ ,
 R. Vazquez Gomez⁴⁴ , P. Vazquez Regueiro⁴⁵ , C. Vázquez Sierra⁴⁵ , S. Vecchi²⁴ ,
 J.J. Velthuis⁵³ , M. Veltri^{25,x} , A. Venkateswaran⁴⁸ , M. Vesterinen⁵⁵ ,
 M. Vieites Diaz⁴⁷ , X. Vilasis-Cardona⁴³ , E. Vilella Figueras⁵⁹ , A. Villa²³ ,
 P. Vincent¹⁵ , F.C. Volle⁵² , D. vom Bruch¹² , N. Voropaev⁴² , K. Vos⁷⁶ ,

G. Vouters¹⁰ , C. Vrahas⁵⁷ , J. Wagner¹⁸ , J. Walsh³³ , E.J. Walton^{1,55} , G. Wan⁶ , C. Wang²⁰ , G. Wang⁸ , J. Wang⁶ , J. Wang⁵ , J. Wang⁴ , J. Wang⁷² , M. Wang²⁸ , N. W. Wang⁷ , R. Wang⁵³ , X. Wang⁸ , X. Wang⁷⁰ , X. W. Wang⁶⁰ , Z. Wang¹³ , Z. Wang⁴ , Z. Wang²⁸ , J.A. Ward^{55,1} , M. Waterlaet⁴⁷ , N.K. Watson⁵² , D. Websdale⁶⁰ , Y. Wei⁶ , J. Wendel⁷⁸ , B.D.C. Westhenry⁵³ , D.J. White⁶¹ , M. Whitehead⁵⁸ , A.R. Wiederhold⁵⁵ , D. Wiedner¹⁸ , G. Wilkinson⁶² , M.K. Wilkinson⁶⁴ , M. Williams⁶³ , M.R.J. Williams⁵⁷ , R. Williams⁵⁴ , F.F. Wilson⁵⁶ , W. Wislicki⁴⁰ , M. Witek³⁹ , L. Witola²⁰ , C.P. Wong⁶⁶ , G. Wormser¹³ , S.A. Wotton⁵⁴ , H. Wu⁶⁷ , J. Wu⁸ , Y. Wu⁶ , K. Wyllie⁴⁷ , S. Xian⁷⁰ , Z. Xiang⁵ , Y. Xie⁸ , A. Xu³³ , J. Xu⁷ , L. Xu⁴ , L. Xu⁴ , M. Xu⁵⁵ , Z. Xu¹¹ , Z. Xu⁷ , Z. Xu⁵ , D. Yang⁴ , S. Yang⁷ , X. Yang⁶ , Y. Yang^{27,n} , Z. Yang⁶ , Z. Yang⁶⁵ , V. Yeroshenko¹³ , H. Yeung⁶¹ , H. Yin⁸ , C. Y. Yu⁶ , J. Yu⁶⁹ , X. Yuan⁵ , E. Zaffaroni⁴⁸ , M. Zavertyaev¹⁹ , M. Zdybal³⁹ , M. Zeng⁴ , C. Zhang⁶ , D. Zhang⁸ , J. Zhang⁷ , L. Zhang⁴ , S. Zhang⁶⁹ , S. Zhang⁶ , Y. Zhang⁶ , Y. Z. Zhang⁴ , Y. Zhao²⁰ , A. Zharkova⁴² , A. Zhelezov²⁰ , X. Z. Zheng⁴ , Y. Zheng⁷ , T. Zhou⁶ , X. Zhou⁸ , Y. Zhou⁷ , V. Zhovkovska⁵⁵ , L. Z. Zhu⁷ , X. Zhu⁴ , X. Zhu⁸ , V. Zhukov¹⁶ , J. Zhuo⁴⁶ , Q. Zou^{5,7} , D. Zuliani^{31,q} , G. Zunica⁴⁸ .

¹*School of Physics and Astronomy, Monash University, Melbourne, Australia*

²*Centro Brasileiro de Pesquisas Físicas (CBPF), Rio de Janeiro, Brazil*

³*Universidade Federal do Rio de Janeiro (UFRJ), Rio de Janeiro, Brazil*

⁴*Center for High Energy Physics, Tsinghua University, Beijing, China*

⁵*Institute Of High Energy Physics (IHEP), Beijing, China*

⁶*School of Physics State Key Laboratory of Nuclear Physics and Technology, Peking University, Beijing, China*

⁷*University of Chinese Academy of Sciences, Beijing, China*

⁸*Institute of Particle Physics, Central China Normal University, Wuhan, Hubei, China*

⁹*Consejo Nacional de Rectores (CONARE), San Jose, Costa Rica*

¹⁰*Université Savoie Mont Blanc, CNRS, IN2P3-LAPP, Annecy, France*

¹¹*Université Clermont Auvergne, CNRS/IN2P3, LPC, Clermont-Ferrand, France*

¹²*Aix Marseille Univ, CNRS/IN2P3, CPPM, Marseille, France*

¹³*Université Paris-Saclay, CNRS/IN2P3, IJCLab, Orsay, France*

¹⁴*Laboratoire Leprince-Ringuet, CNRS/IN2P3, Ecole Polytechnique, Institut Polytechnique de Paris, Palaiseau, France*

¹⁵*LPNHE, Sorbonne Université, Paris Diderot Sorbonne Paris Cité, CNRS/IN2P3, Paris, France*

¹⁶*I. Physikalisches Institut, RWTH Aachen University, Aachen, Germany*

¹⁷*Universität Bonn - Helmholtz-Institut für Strahlen und Kernphysik, Bonn, Germany*

¹⁸*Fakultät Physik, Technische Universität Dortmund, Dortmund, Germany*

¹⁹*Max-Planck-Institut für Kernphysik (MPIK), Heidelberg, Germany*

²⁰*Physikalisches Institut, Ruprecht-Karls-Universität Heidelberg, Heidelberg, Germany*

²¹*School of Physics, University College Dublin, Dublin, Ireland*

²²*INFN Sezione di Bari, Bari, Italy*

²³*INFN Sezione di Bologna, Bologna, Italy*

²⁴*INFN Sezione di Ferrara, Ferrara, Italy*

²⁵*INFN Sezione di Firenze, Firenze, Italy*

²⁶*INFN Laboratori Nazionali di Frascati, Frascati, Italy*

²⁷*INFN Sezione di Genova, Genova, Italy*

²⁸*INFN Sezione di Milano, Milano, Italy*

²⁹*INFN Sezione di Milano-Bicocca, Milano, Italy*

³⁰*INFN Sezione di Cagliari, Monserrato, Italy*

³¹*INFN Sezione di Padova, Padova, Italy*

³²*INFN Sezione di Perugia, Perugia, Italy*

³³*INFN Sezione di Pisa, Pisa, Italy*

³⁴*INFN Sezione di Roma La Sapienza, Roma, Italy*

³⁵*INFN Sezione di Roma Tor Vergata, Roma, Italy*

- ³⁶ *Nikhef National Institute for Subatomic Physics, Amsterdam, Netherlands*
- ³⁷ *Nikhef National Institute for Subatomic Physics and VU University Amsterdam, Amsterdam, Netherlands*
- ³⁸ *AGH - University of Krakow, Faculty of Physics and Applied Computer Science, Kraków, Poland*
- ³⁹ *Henryk Niewodniczanski Institute of Nuclear Physics Polish Academy of Sciences, Kraków, Poland*
- ⁴⁰ *National Center for Nuclear Research (NCBJ), Warsaw, Poland*
- ⁴¹ *Horia Hulubei National Institute of Physics and Nuclear Engineering, Bucharest-Magurele, Romania*
- ⁴² *Affiliated with an institute covered by a cooperation agreement with CERN*
- ⁴³ *DS4DS, La Salle, Universitat Ramon Llull, Barcelona, Spain*
- ⁴⁴ *ICCUB, Universitat de Barcelona, Barcelona, Spain*
- ⁴⁵ *Instituto Galego de Física de Altas Enerxías (IGFAE), Universidade de Santiago de Compostela, Santiago de Compostela, Spain*
- ⁴⁶ *Instituto de Física Corpuscular, Centro Mixto Universidad de Valencia - CSIC, Valencia, Spain*
- ⁴⁷ *European Organization for Nuclear Research (CERN), Geneva, Switzerland*
- ⁴⁸ *Institute of Physics, Ecole Polytechnique Fédérale de Lausanne (EPFL), Lausanne, Switzerland*
- ⁴⁹ *Physik-Institut, Universität Zürich, Zürich, Switzerland*
- ⁵⁰ *NSC Kharkiv Institute of Physics and Technology (NSC KIPT), Kharkiv, Ukraine*
- ⁵¹ *Institute for Nuclear Research of the National Academy of Sciences (KINR), Kyiv, Ukraine*
- ⁵² *University of Birmingham, Birmingham, United Kingdom*
- ⁵³ *H.H. Wills Physics Laboratory, University of Bristol, Bristol, United Kingdom*
- ⁵⁴ *Cavendish Laboratory, University of Cambridge, Cambridge, United Kingdom*
- ⁵⁵ *Department of Physics, University of Warwick, Coventry, United Kingdom*
- ⁵⁶ *STFC Rutherford Appleton Laboratory, Didcot, United Kingdom*
- ⁵⁷ *School of Physics and Astronomy, University of Edinburgh, Edinburgh, United Kingdom*
- ⁵⁸ *School of Physics and Astronomy, University of Glasgow, Glasgow, United Kingdom*
- ⁵⁹ *Oliver Lodge Laboratory, University of Liverpool, Liverpool, United Kingdom*
- ⁶⁰ *Imperial College London, London, United Kingdom*
- ⁶¹ *Department of Physics and Astronomy, University of Manchester, Manchester, United Kingdom*
- ⁶² *Department of Physics, University of Oxford, Oxford, United Kingdom*
- ⁶³ *Massachusetts Institute of Technology, Cambridge, MA, United States*
- ⁶⁴ *University of Cincinnati, Cincinnati, OH, United States*
- ⁶⁵ *University of Maryland, College Park, MD, United States*
- ⁶⁶ *Los Alamos National Laboratory (LANL), Los Alamos, NM, United States*
- ⁶⁷ *Syracuse University, Syracuse, NY, United States*
- ⁶⁸ *Pontifícia Universidade Católica do Rio de Janeiro (PUC-Rio), Rio de Janeiro, Brazil, associated to ³*
- ⁶⁹ *School of Physics and Electronics, Hunan University, Changsha City, China, associated to ⁸*
- ⁷⁰ *Guangdong Provincial Key Laboratory of Nuclear Science, Guangdong-Hong Kong Joint Laboratory of Quantum Matter, Institute of Quantum Matter, South China Normal University, Guangzhou, China, associated to ⁴*
- ⁷¹ *Lanzhou University, Lanzhou, China, associated to ⁵*
- ⁷² *School of Physics and Technology, Wuhan University, Wuhan, China, associated to ⁴*
- ⁷³ *Departamento de Física, Universidad Nacional de Colombia, Bogota, Colombia, associated to ¹⁵*
- ⁷⁴ *Eotvos Lorand University, Budapest, Hungary, associated to ⁴⁷*
- ⁷⁵ *Van Swinderen Institute, University of Groningen, Groningen, Netherlands, associated to ³⁶*
- ⁷⁶ *Universiteit Maastricht, Maastricht, Netherlands, associated to ³⁶*
- ⁷⁷ *Tadeusz Kosciuszko Cracow University of Technology, Cracow, Poland, associated to ³⁹*
- ⁷⁸ *Universidade da Coruña, A Coruna, Spain, associated to ⁴³*
- ⁷⁹ *Department of Physics and Astronomy, Uppsala University, Uppsala, Sweden, associated to ⁵⁸*
- ⁸⁰ *University of Michigan, Ann Arbor, MI, United States, associated to ⁶⁷*
- ⁸¹ *Departement de Physique Nucleaire (SPhN), Gif-Sur-Yvette, France*

^a *Universidade de Brasília, Brasília, Brazil*

^b *Centro Federal de Educação Tecnológica Celso Suckow da Fonseca, Rio De Janeiro, Brazil*

^c *Hangzhou Institute for Advanced Study, UCAS, Hangzhou, China*

^d *School of Physics and Electronics, Henan University, Kaifeng, China*

^e *LIP6, Sorbonne Université, Paris, France*

^f *Excellence Cluster ORIGINS, Munich, Germany*

^g *Universidad Nacional Autónoma de Honduras, Tegucigalpa, Honduras*

^h *Università di Bari, Bari, Italy*

ⁱ *Università degli studi di Bergamo, Bergamo, Italy*

^j *Università di Bologna, Bologna, Italy*

^k *Università di Cagliari, Cagliari, Italy*

^l *Università di Ferrara, Ferrara, Italy*

^m *Università di Firenze, Firenze, Italy*

ⁿ *Università di Genova, Genova, Italy*

^o *Università degli Studi di Milano, Milano, Italy*

^p *Università degli Studi di Milano-Bicocca, Milano, Italy*

^q *Università di Padova, Padova, Italy*

^r *Università di Perugia, Perugia, Italy*

^s *Scuola Normale Superiore, Pisa, Italy*

^t *Università di Pisa, Pisa, Italy*

^u *Università della Basilicata, Potenza, Italy*

^v *Università di Roma Tor Vergata, Roma, Italy*

^w *Università di Siena, Siena, Italy*

^x *Università di Urbino, Urbino, Italy*

^y *Universidad de Alcalá, Alcalá de Henares, Spain*

^z *Facultad de Ciencias Físicas, Madrid, Spain*

^{aa} *Department of Physics/Division of Particle Physics, Lund, Sweden*

[†] *Deceased*